nature nanotechnology

Article

https://doi.org/10.1038/s41565-023-01543-8

Efficient multicarbon formation in acidic CO_2 reduction via tandem electrocatalysis

In the format provided by the authors and unedited

Efficient multicarbon formation in acidic CO_2 reduction via tandem electrocatalysis

Authors: Yuanjun Chen[1,8], Xiao-Yan Li[1,8], Zhu Chen[1,8], Adnan Ozden[2], Jianan Erick Huang[1], Pengfei Ou[1], Juncai Dong[3], Jinqiang Zhang[1], Cong Tian[1], Byoung-Hoon Lee[1,7], Xinyue Wang[1], Shijie Liu[2], Qingyun Qu[4], Sasa Wang[1], Yi Xu[2], Rui Kai Miao[2], Yong Zhao[2], Yanjiang Liu[1], Chenyue Qiu[5], Jehad Abed[1], Hengzhou Liu[6], Heejong Shin[6], Dingsheng Wang[4], Yadong Li[4], David Sinton[2] and Edward H. Sargent[1*]

Affiliations:

[1]Department of Electrical and Computer Engineering, University of Toronto, Toronto, ON M5S 1A4 Canada.

[2]Department of Mechanical and Industrial Engineering, University of Toronto, Toronto, ON M5S 3G8, Canada.

[3]Beijing Synchrotron Radiation Facility, Institute of High Energy Physics, Chinese Academy of Sciences, Beijing 100049, China.

[4]Department of Chemistry, Tsinghua University, Beijing 100084, China.

[5]Department of Materials Science and Engineering, University of Toronto, Toronto, ON M5S 3E4, Canada.

[6]Department of Chemistry, Northwestern University, 2145 Sheridan Road, Evanston, Illinois, 60208, United States.

[7]KU-KIST Graduate School of Converging Science and Technology, Korea University, 145 Anam-ro, Seongbuk-gu, Seoul 02841, Republic of Korea.

[8]These authors contributed equally: Yuanjun Chen, Xiao-Yan Li, Zhu Chen

*Corresponding author. Email: ted.sargent@utoronto.ca (E.H.S)

This PDF file includes:

Supplementary Figures 1-68

Supplementary Notes 1-12

Supplementary Tables 1-6

Supplementary References

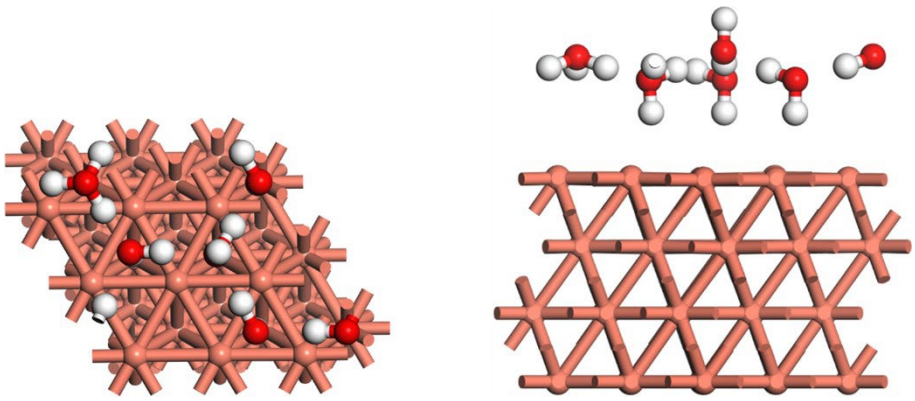

Supplementary Figure 1 | The periodic model of Cu(111) covered a layer of water consisting of five water molecules and one hydronium molecule. Cu: orange; O: Red; H: white.

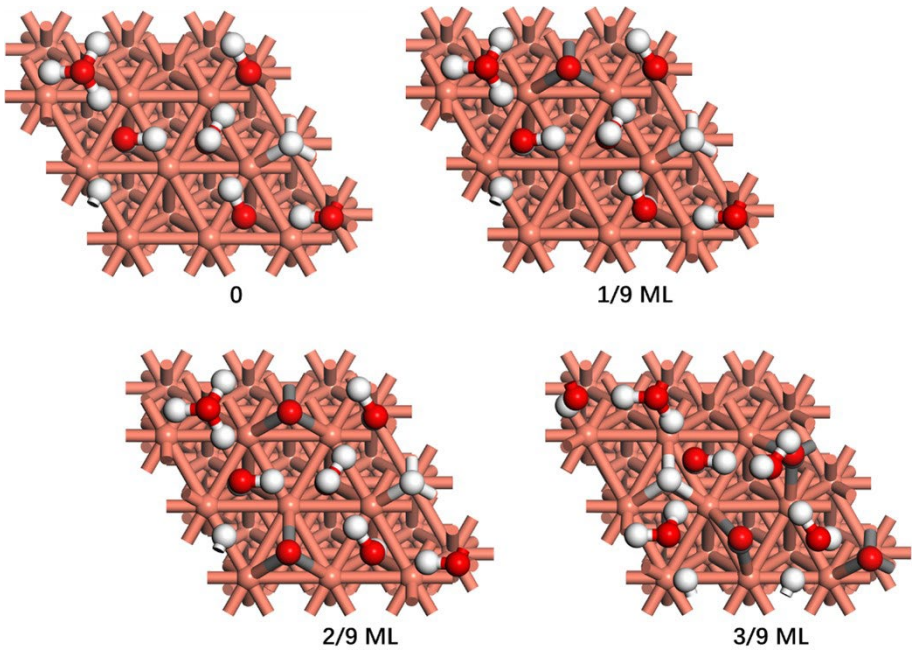

Supplementary Figure 2 | The optimized structures of *H adsorption on Cu(111) at the CO coverage of 2/9 ML, 3/9 ML, 4/9 ML. Cu: orange; O: Red; H: white; C: grey.

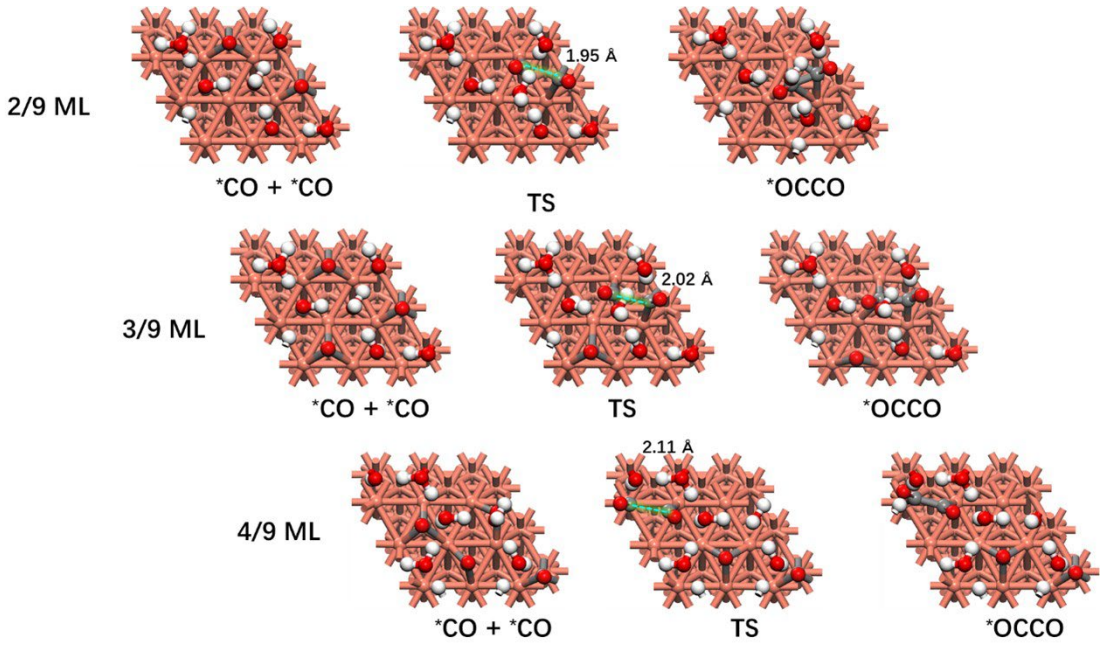

Supplementary Figure 3 | The initial, transitional, and final states of C-C coupling on Cu(111) at the CO coverage of 2/9 ML, 3/9 ML, and 4/9 ML. The distances of C-C in the transition states are plotted and labeled. TS refers to the transitional state. Cu: orange; O: Red; H: white; C: grey.

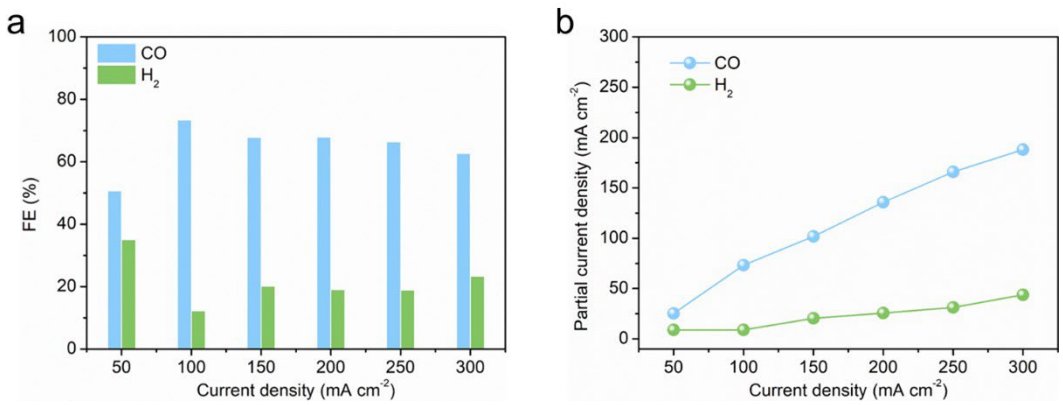

Supplementary Figure 4 | Acidic CO_2RR performance of the state-of-the-art carbon-supported cobalt phthalocyanine (CoPc/C) catalyst at 25 ℃. a, CO and H_2 FE on CoPc/C catalyst at various current densities in the acidic buffer electrolyte of 0.5 M H_3PO_4 and 0.5 M KH_2PO_4 with 2.5 M KCl. **b**, The partial current densities of CO and H_2 on CoPc/C catalyst at various current density in the acidic buffer electrolyte of 0.5 M H_3PO_4 and 0.5 M KH_2PO_4 with 2.5 M KCl.

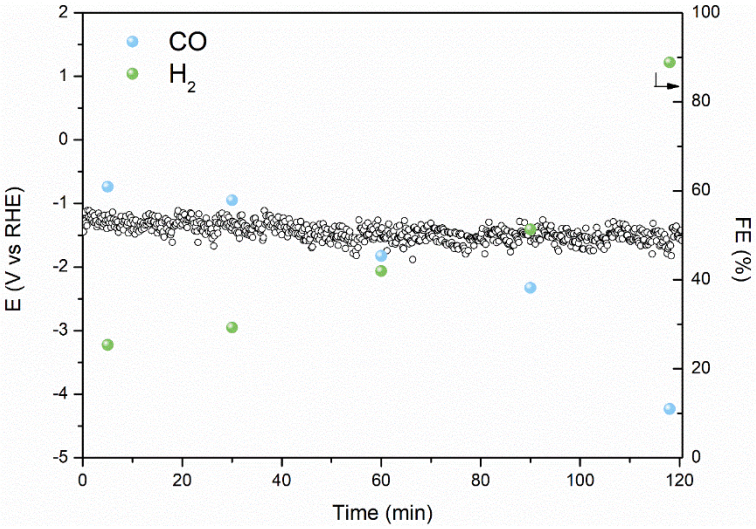

Supplementary Figure 5 | The stability test of the CoPc/C catalyst at the current density of 300 mA cm^{-2} in acidic CO_2RR in the acidic buffer electrolyte of 0.5 M H_3PO_4 and 0.5 M KH_2PO_4 with 2.5 M KCl at 25 ℃.

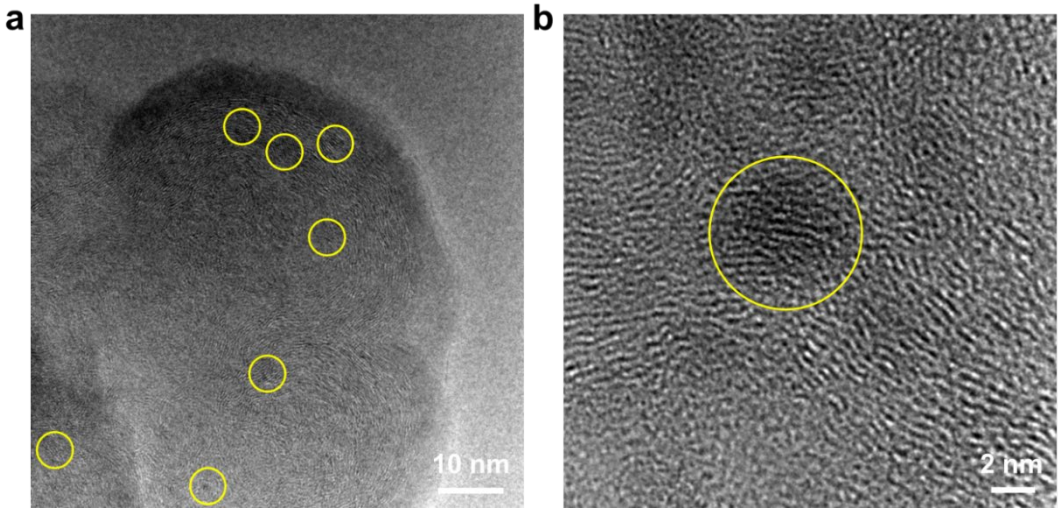

Supplementary Figure 6 | High-resolution transmission electrode microscopy (HRTEM) images of the CoPc/C catalyst after the stability test. The nanoparticles were observed in the post-reaction CoPc/C catalyst, suggesting the agglomeration of CoPc into Co clusters and small-size Co nanoparticles after the stability test. This is particularly important since the Co cation can decrease in oxidation state under cathodic potential in acidic conditions: $[Co^{II}Pc]^0$ → $[Co^{I}Pc]^-$, and when this occurs, doming/bowing of the molecular complex can occur, making it easier to release from the surface[1,2].

Supplementary Note 1| Structure characterization of CoPc@HC

Scanning electron microscopy (SEM) and transmission electron microscopy (TEM) images show that CoPc@HC displays a uniform hollow polyhedral morphology (Fig. 2b and Supplementary Figs. 7-8). High-angle annular dark-field scanning TEM (HAADF-SETM) image detects no agglomeration of CoPc, and the corresponding energy-dispersive X-ray spectroscopy (EDS) mappings reveal uniform distribution of Co species throughout the entire N, P, and S co-doped hollow carbon polyhedron architecture (Fig. 2c). The Co content in CoPc@HC was determined by inductively coupled plasma optical emission spectrometry (ICP-OES) as 0.44 wt%, corresponding to 4.3 wt% of CoPc in CoPc@HC. No obvious diffraction peaks assigned to CoPc were observed in the powder X-ray diffraction (PXRD) pattern of CoPc@HC (Supplementary Fig. 9). The above results suggest CoPc molecules possess a good dispersion on HC. Furthermore, aberration-corrected HAADF-STEM measurement was performed to directly observe the dispersion of CoPc at the atomic level, indicating that CoPc molecules were atomically dispersed on N, P, and S co-doped hollow carbon polyhedron (Fig. 2d).

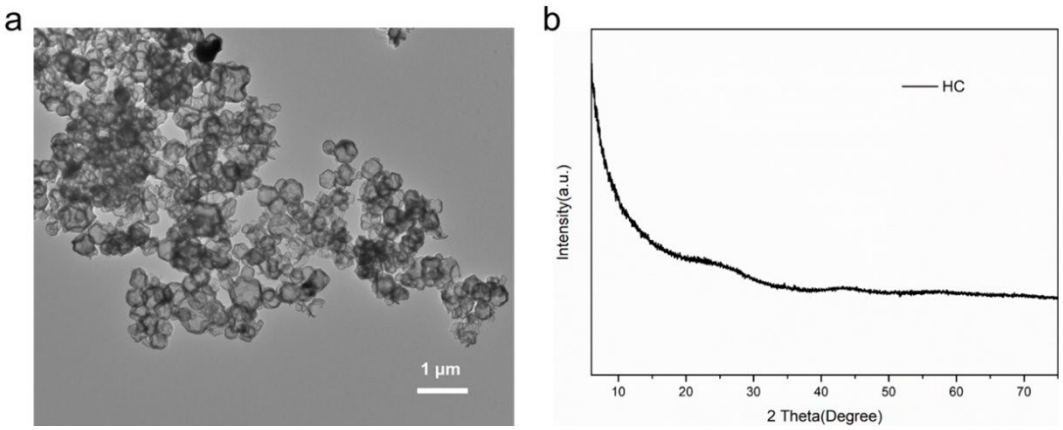

Supplementary Figure 7 | Structural characterization of N, P, S co-doped hollow carbon (HC). a, Transmission electron microscopy (TEM) image of HC. **b**, Powder X-ray diffraction (XRD) pattern (b) of HC.

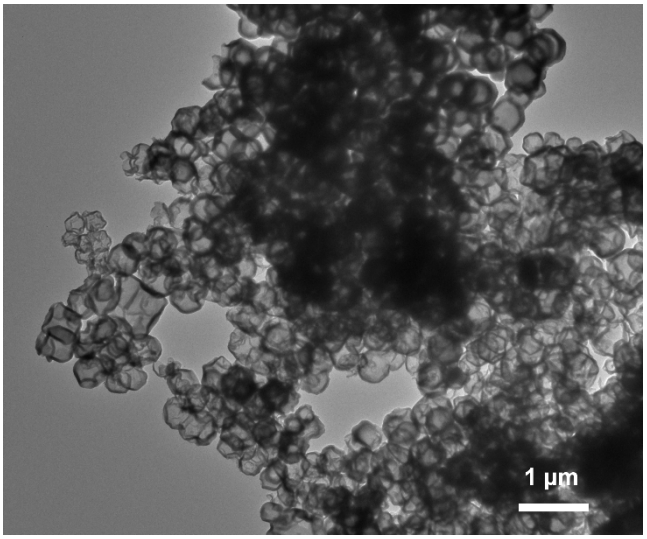

Supplementary Figure 8 | Transmission electron microscopy (TEM) image of CoPc@HC.

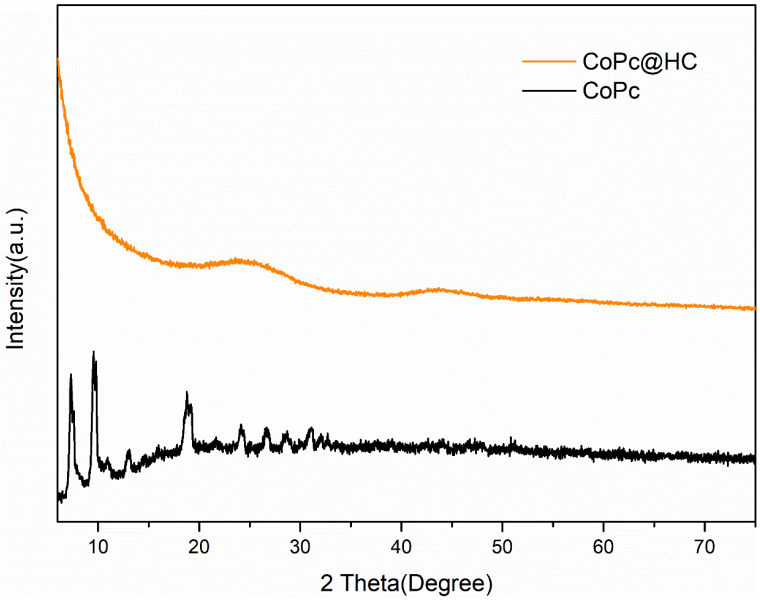

Supplementary Figure 9 | Powder X-ray diffraction (XRD) pattern of CoPc@HC in comparison to CoPc molecules.

Supplementary Note 2| Strong catalyst-support interaction in CoPc@HC

Synchrotron-radiation-based X-ray absorption fine structure (XAS) analysis was carried out to investigate the electronic structure and coordination environment. Fig. 2e shows the X-ray absorption near-edge structure (XANES) spectra of CoPc@HC and references. The XANES curve of CoPc@HC exhibits a higher absorption-edge energy compared with pure CoPc (Supplementary Fig. 10), suggesting the electron-deficient nature of the Co center of CoPc@HC. The Co K-edge white-line peak is generated by the transition from the 1s to 4p unoccupied states. A higher intensity of the white-line peak indicates more electron transfer from metal center atom to the coordination atoms. For CoPc@HC, it can be observed that the white-line peak locates at approximately 7130 eV with a higher intensity compared to that of pure CoPc, which is attributed to the strong electronic interaction between CoPc and the N species of the HC substrate, suggesting that the electron transfers from the Co species of CoPc@HC to the N in the HC support. These findings suggest a strong electronic interaction between CoPc and the N species of HC substrate. As shown in Fig. 2f, the Co K-edge of CoPc@HC catalyst exhibits a similar Fourier transformed (FT) extended X-ray absorption fine structure (FT-EXAFS) spectrum to that of CoPc, suggesting the main peak observed in approximately 1.3 Å is associated with the Co-N coordination. Furthermore, the wavelet transform (WT) contour plot of CoPc@HC displays one intensity maximum at about 4.3 $Å^{-1}$, associated with the contribution of Co-N scattering path by comparing with the WT analysis of CoPc, Co foil, CoO and Co_3O_4 (Supplementary Fig. 11). The intensity maximum at about 6.8 $Å^{-1}$ indexed to Co-Co coordination is not detected in CoPc@HC. Quantitative least-squares EXAFS curve-fitting analysis was performed to extract the coordination configuration (Supplementary Figs. 12-16). The first-shell EXAFS curve-fitting result of CoPc@HC reveals that the main peak at 1.3 Å is attributed to the superimposition of the Co-N_4 coordination from CoPc molecules and Co-N coordination from the interaction between CoPc molecules and HC substrate (Supplementary Table 1). The above analysis reveals that strong electronic interaction between CoPc and the N species of HC substrate contributes to the atomic dispersion and stabilization of CoPc molecules.

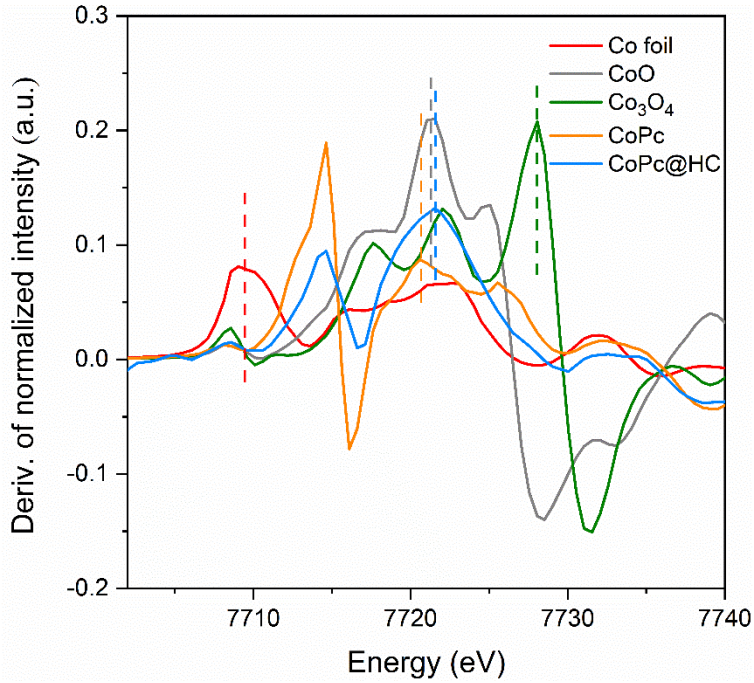

Supplementary Figure 10 | The first derivative curves of CoPc@HC and reference samples. The first derivative curves demonstrate that Co species in CoPc@HC exhibit a higher oxidation state compared to pure CoPc, suggesting the electron-deficient nature of the Co center of CoPc@HC, ascribed to the strong electronic interaction between CoPc and the N species of HC substrate.

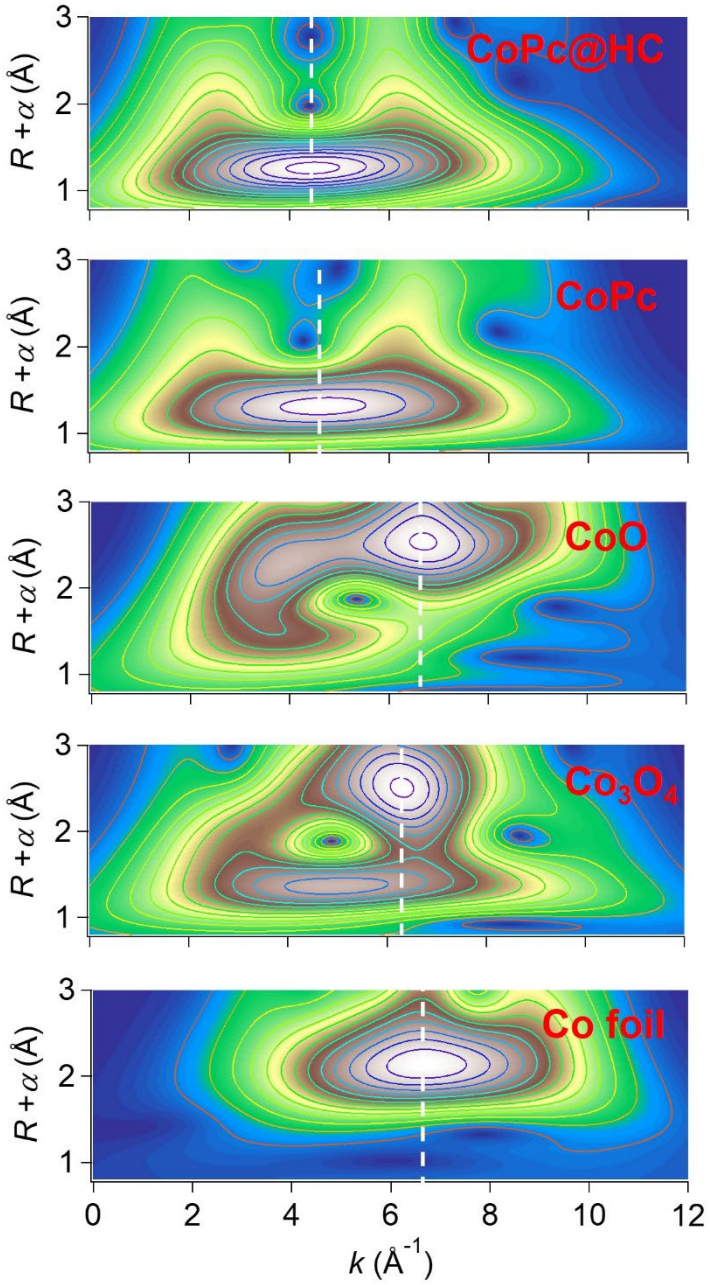

Supplementary Figure 11 | Co K-edge wavelet transformed extended X-ray absorption fine structure (WT-EXAFS) contour plots of CoPc@HC and reference samples (CoPc, CoO, Co_3O_4, and Co foil).

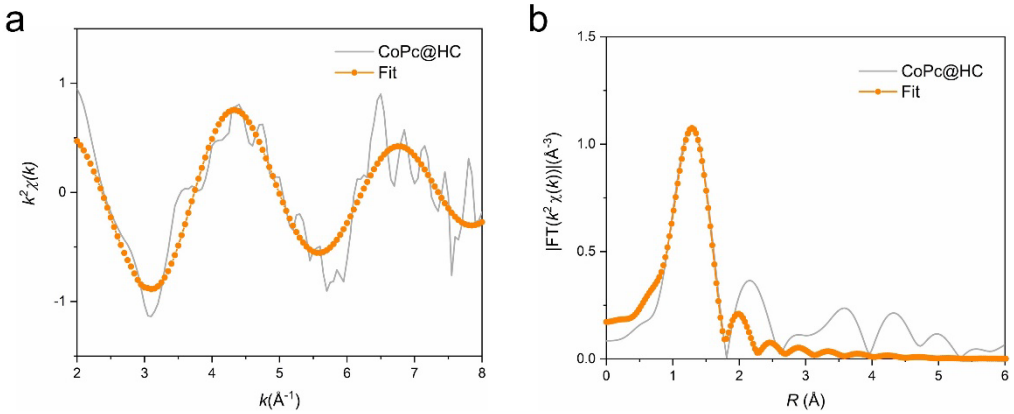

Supplementary Figure 12 | Co K-edge EXAFS first-shell fitting analysis of CoPc@HC in *k* space (a) and (b) *R* space.

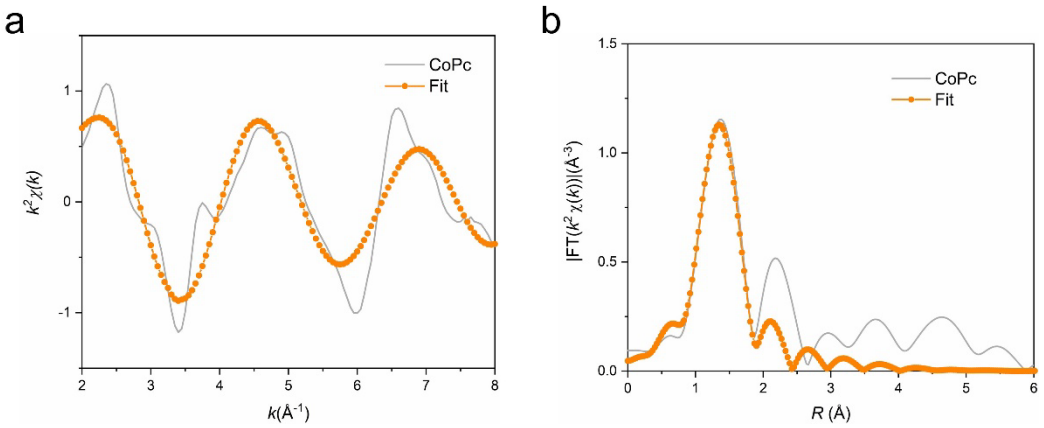

Supplementary Figure 13 | Co K-edge EXAFS first-shell fitting analysis of CoPc in *k* space (a) and (b) *R* space.

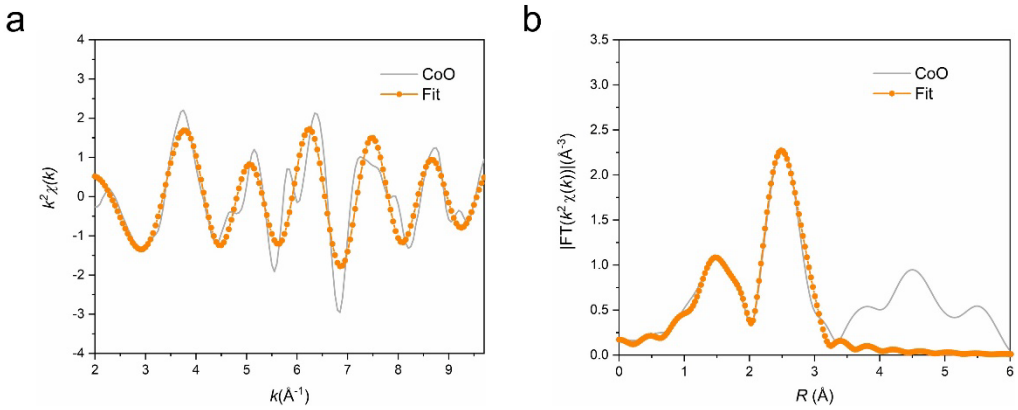

Supplementary Figure 14 | Co K-edge EXAFS fitting analysis of CoO in *k* space (a) and (b) *R* space.

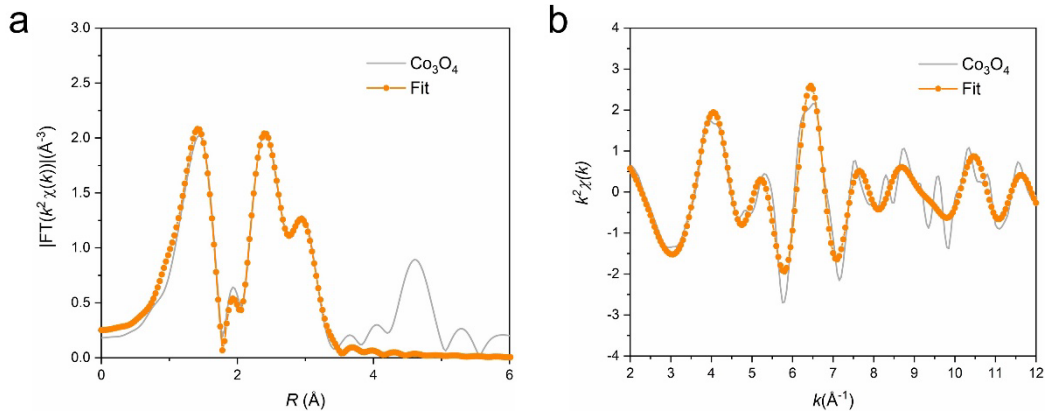

Supplementary Figure 15 | Co K-edge EXAFS fitting analysis of Co_3O_4 in *k* space (a) and (b) *R* space.

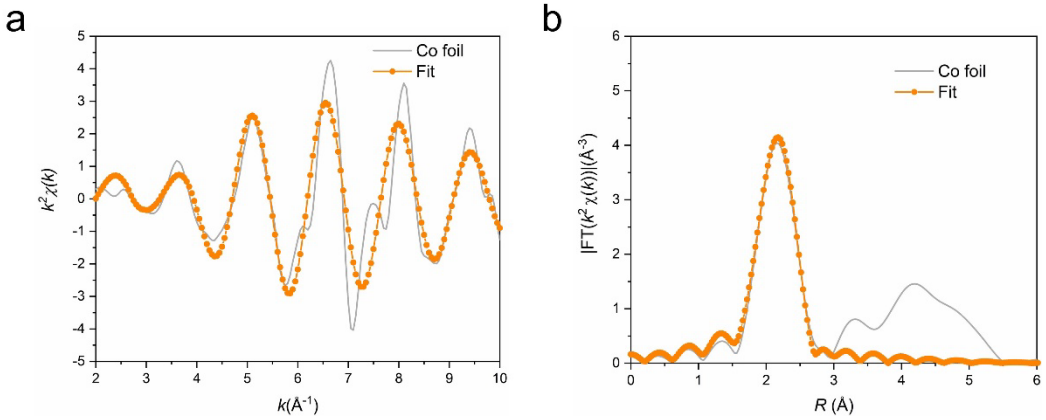

Supplementary Figure 16 | Co K-edge EXAFS fitting analysis of Co foil in *k* space (a) and (b) *R* space.

Supplementary Table 1 | Co K-edge EXAFS curve Fitting Parameters[a].

sample	path	N	R (Å)	σ^2 (Å^2)
Co foil[b]	Co-Co	12	2.49	0.008
CoO[c]	Co-O	6	2.11	0.010
	Co-Co	12	2.99	0.009
Co_3O_4[d]	Co-O	5.3	1.92	0.005
	Co-Co	4	2.85	0.004
	Co-Co	8	3.36	0.007
CoPc[e]	Co-N	4.2	1.88	0.007
CoPc@HC[f]	Co-N	5.3	1.87	0.008

[a]*N*, coordination number; *R*, distance between absorber and backscatter atoms; σ^2, Debye–Waller factor to account for both thermal and structural disorders; Error bounds (accuracies) that characterize the structural parameters obtained by EXAFS spectroscopy were estimated as N ± 20%; R ± 1%; σ^2 ± 20%. S_0^2 was fixed to 0.93 as determined from Co foil fitting. [b]Fitting range: $2 \le k$ (/Å) ≤ 10 and $1 \le R$ (Å) ≤ 3. [c]Fitting range: $2.0 \le k$ (/Å) ≤ 9.7 and $1.0 \le R$ (Å) ≤ 3. [d]Fitting range: $2.0 \le k$ (/Å) ≤ 12.0 and $1.0 \le R$ (Å) ≤ 3.50. [e]Fitting range: $2.0 \le k$ (/Å) ≤ 8.0 and $1.0 \le R$ (Å) ≤ 1.9. [f]Fitting range: $2.0 \le k$ (/Å) ≤ 8.0 and $1.0 \le R$ (Å) ≤ 2.0.

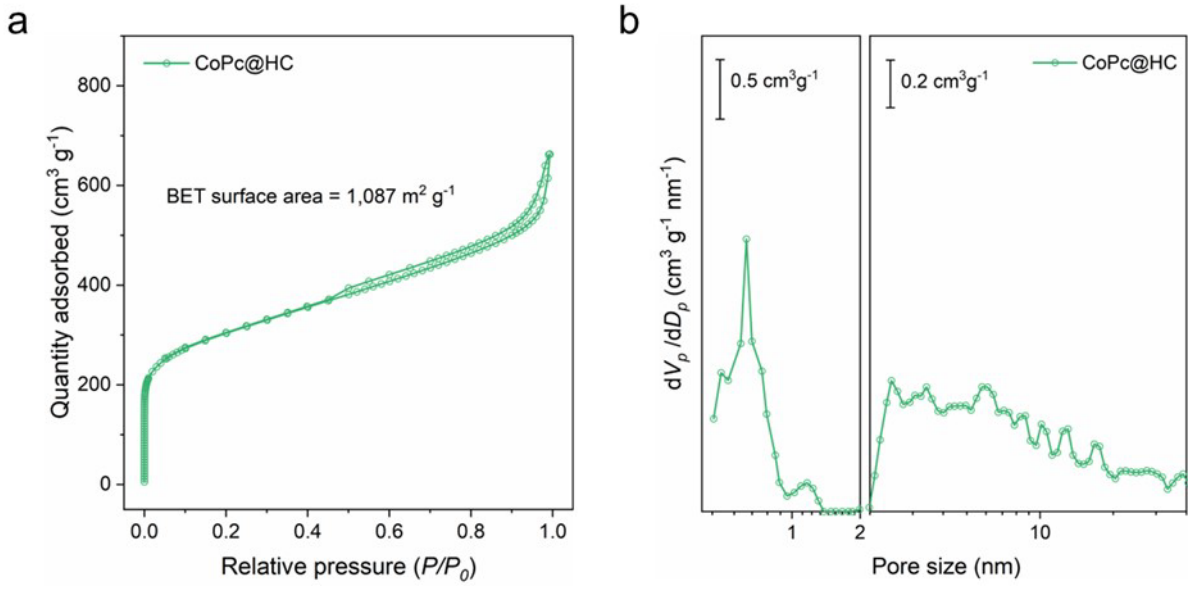

Supplementary Figure 17 | The porous structure of the CoPc@HC catalyst. a, Nitrogen adsorption/desorption isotherms. **b**, The pore distribution of micropore (< 2 nm) and mesopore (2~10 nm).

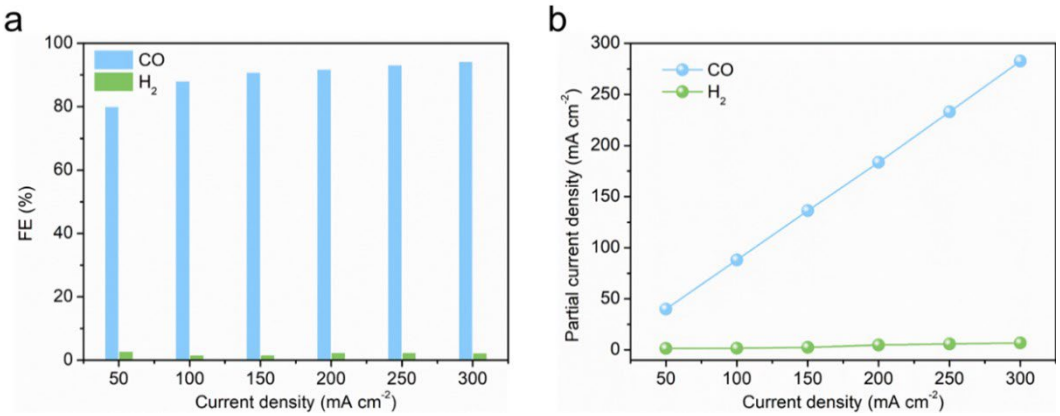

Supplementary Figure 18 | Acidic CO_2RR performance of the CoPc@HC catalyst at 25 °C. a, CO and H_2 FE on CoPc@HC in acidic CO_2RR at various current densities in the acidic buffer electrolyte of 0.5 M H_3PO_4 and 0.5 M KH_2PO_4 with 2.5 M KCl. **b**, The partial current density of CO and H_2 on CoPc@HC in acidic CO_2RR in the acidic buffer electrolyte of 0.5 M H_3PO_4 and 0.5 M KH_2PO_4 with 2.5 M KCl.

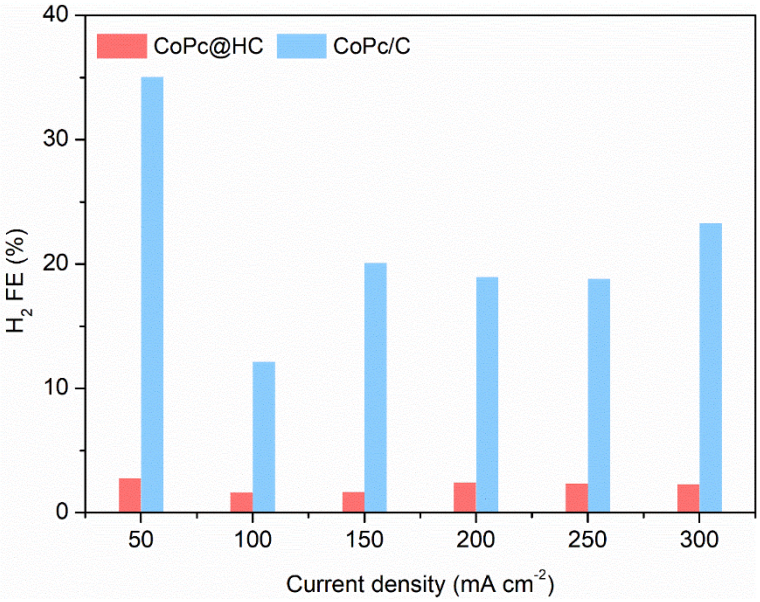

Supplementary Figure 19 | H_2 FE on CoPc@HC electrode and CoPc/C electrode in acidic CO_2RR at different current densities at 25 ℃.

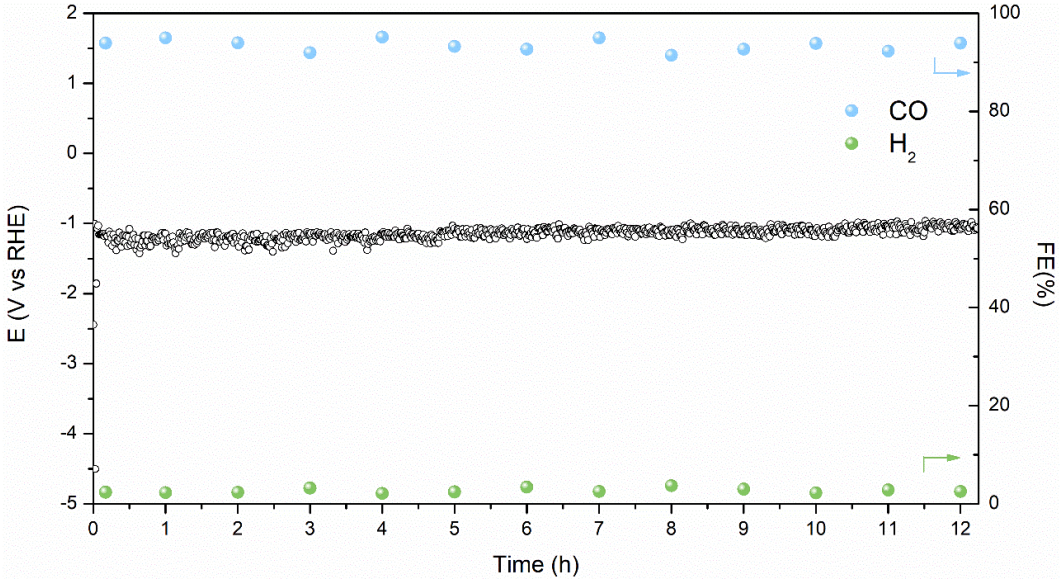

Supplementary Figure 20 | The stability test of CoPc@HC at the current density of 300 mA cm^{-2} in acidic CO_2RR in the acidic buffer electrolyte of 0.5 M H_3PO_4 and 0.5 M KH_2PO_4 with 2.5 M KCl at 25 ℃.

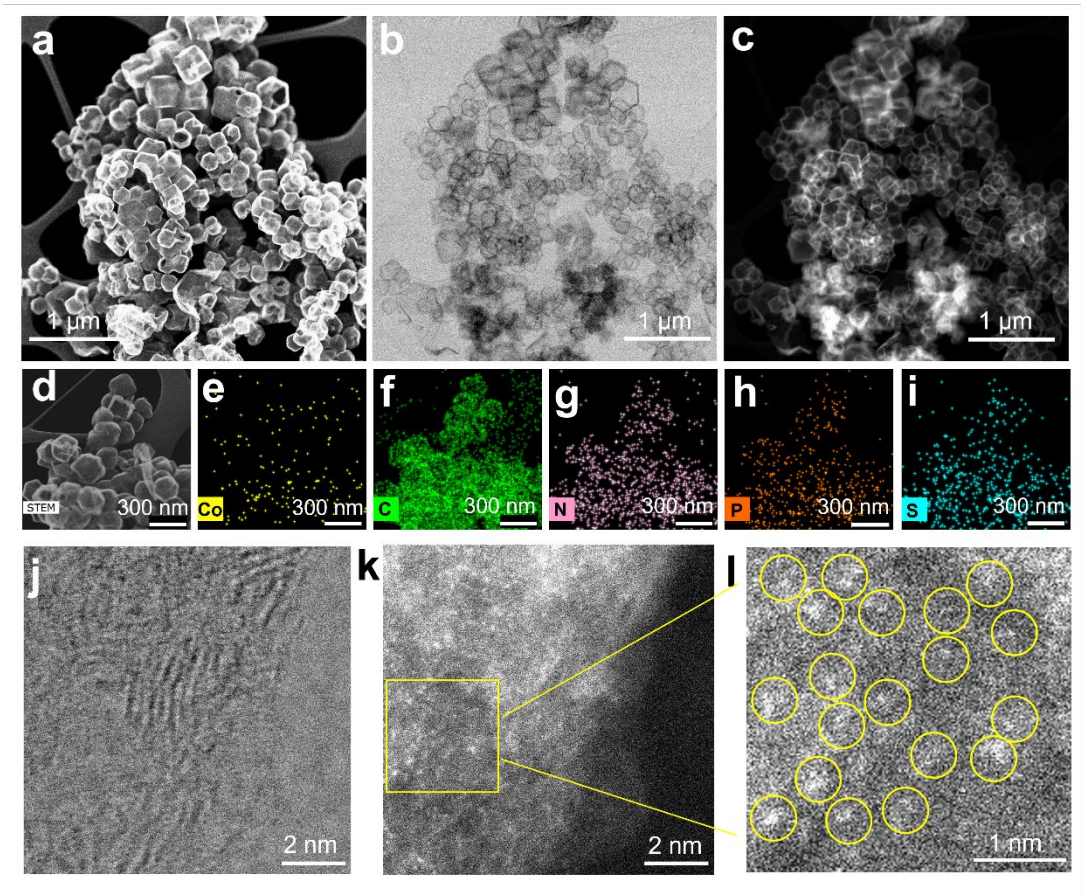

Supplementary Figure 21 | Structural characterizations of the used CoPc@HC sample after a 12 h stability test. **a-c**, STEM secondary electron image (**a**), STEM-bright-field image (**b**) and HAADF-STEM image of the post-reaction CoPc@HC sample. **d-i**, HAADF-STEM image (**d**) and the corresponding EDS mappings of the post-reaction CoPc@HC sample. **j-l**, HRTEM image (**j**), aberration-corrected HAADF-STEM image (**k**) and enlarged image of the post-reaction CoPc@HC sample (**l**).

STEM secondary electron, STEM-bright-field and HAADF-STEM images of the used CoPc@HC sample show the well-preserved hollow morphology and structure as the pristine CoPc@HC. The corresponding EDS images of the used CoPc@HC sample show that Co element uniformly distributes throughout the entire supports. The aberration-corrected TEM image suggests that no evidence of CoPc agglomeration. The aberration-corrected HAADF-STEM image of the used CoPc@HC shows the Co single atoms are identified as the bright dots, which are marked by yellow circles. The findings suggest that the structure of CoPc is well-preserved, demonstrating the high stability of CoPc on HC support.

Supplementary Table 2 | Comparison of CoPc@HC and previously reported catalysts toward the conversion of CO_2 to CO in acidic media at 25 °C.

Electrode	CO FE (%)	Current density ($mA\ cm^{-2}$)	Electrode mass loading (mg/cm^2)	Reference
CoPc@HC	94	300	0.5	This work
Au/C	91*	250	N/A	*Nat. Catal.* **5**, 268-276 (2022)
Au/C	90*	100	2	*Nat. Commun.* **12**, 4943 (2021)
sputtered Ag/PTFE	32	400	N/A	*Science* **372**, 1074-1078 (2021)
Ag	60*	100	16	*ACS Energy Lett.* **6**, 4291-4298 (2021)

*The FE value represents an average.

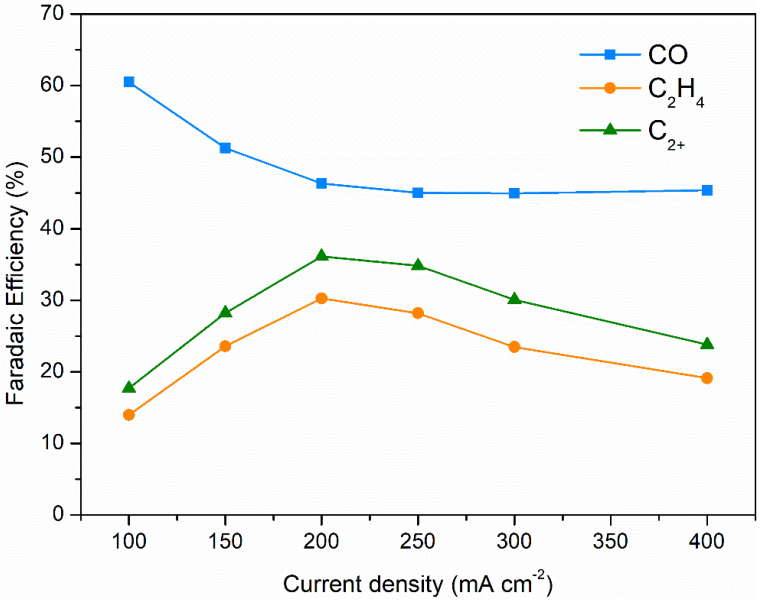

Supplementary Figure 22 | FEs of CO, C_2H_4, and C_{2+} on CoPc@HC/sCu tandem electrode in an acidic buffer electrolyte of 0.5 M H_3PO_4 and 0.5 M KH_2PO_4 with 2.5 M KCl. The flow rate of inlet CO_2 is 10 sccm. The testing temperature is 25 °C.

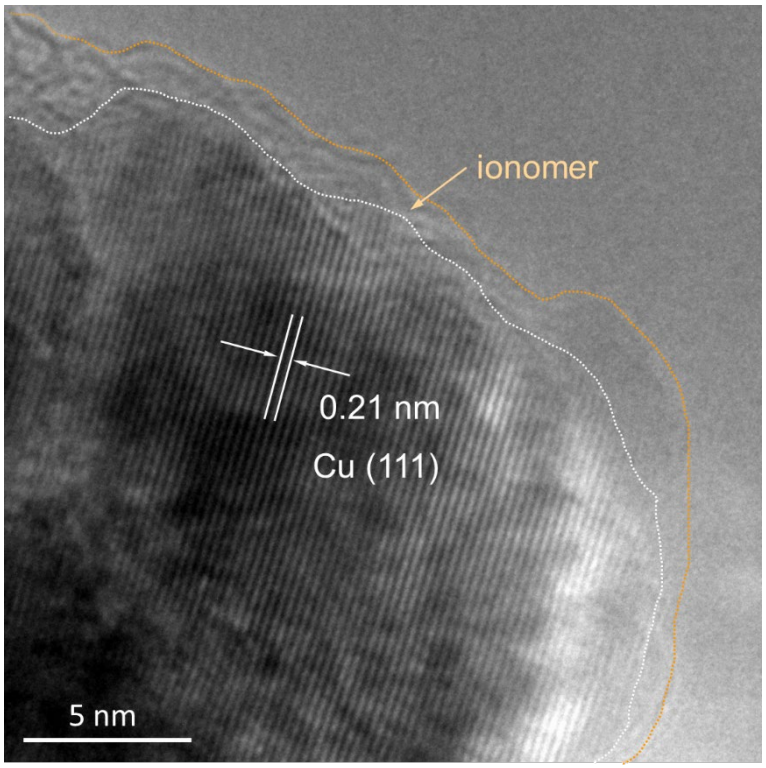

Supplementary Figure 23 | HRTEM image of three-dimensional Cu/ionomer interface catalyst layer reveals that Cu nanoparticles are coated by 1-2 nm continuous and conformal perfluoro sulfonic acid (PFSA) ionomer layer with abundant Cu/ionomer interface.

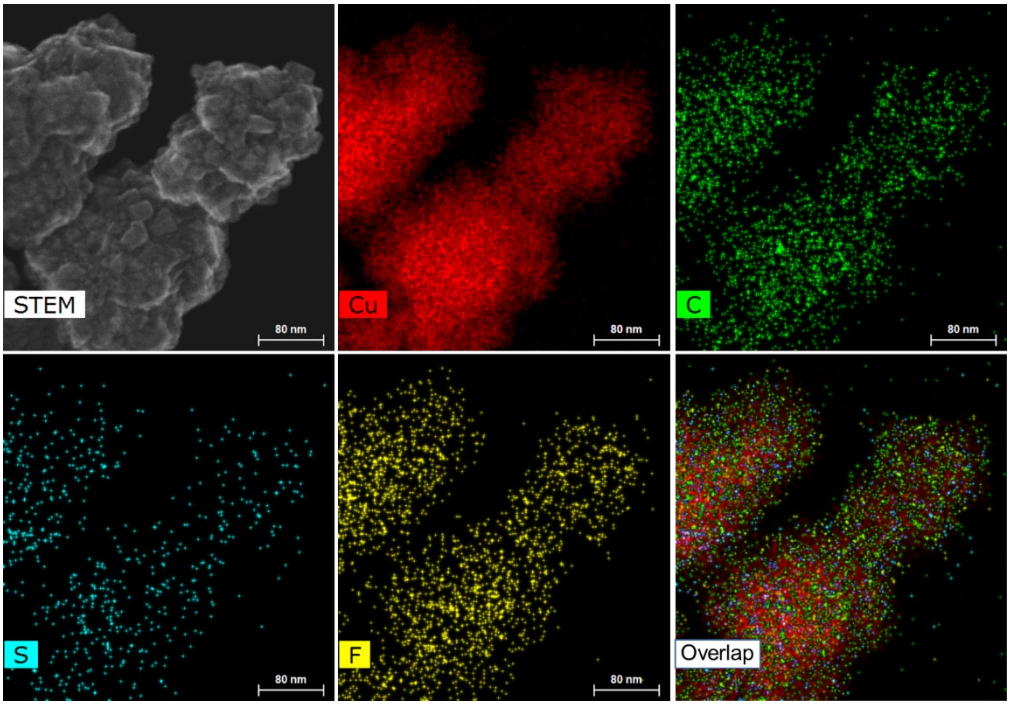

Supplementary Figure 24 | HAADF-STEM image and the corresponding elemental energy-dispersive X-ray spectroscopy (EDS) mapping images of three-dimensional Cu/ionomer interface catalyst layer (Cu, red; C, green; S, light blue; F, yellow). Perfluoro sulfonic acid (PFSA) ionomer exhibits differentiated hydrophilic and hydrophobic characteristics endowed by $-SO_3^-$ and $-CF_2$ functionalities, respectively. The elemental EDS mapping images reveal that the presence of continuous ionomer coating on Cu nanoparticles.

Supplementary Note 3 | The optimization of CoPc@HC/Cu tandem electrode.

We optimized the size of Cu nanoparticles (Cu NP) for the Cu catalyst layer. The commercial Cu NP with 25 nm, 100 nm, and 580 nm coated by perfluoro sulfonic acid (PFSA) ionomer were used as the Cu catalyst layers of tandem electrode and were assessed in acidic CO_2RR system, respectively (Supplementary Fig. 25). The results showed that the 25 nm Cu nanoparticles exhibited the highest C_2H_4 FE and the lowest H_2 FE.

We then conducted the experiments by replacing PFSA with anionic ionomers (Sustainion® XA-9 and Sustainion® XC-2, purchased from Dioxide Materials). At low current densities (<600 mA cm^{-2}), the anionic ionomers displayed a lower H_2 FE and a higher C_2H_4 FE than PFSA (Supplementary Fig. 26). This may relate to their promoting OH^- diffusion and suppressing K^+ and proton diffusion. We also noted that XA-9 exhibited better performance than XC-2. This may be due to a lower ion-exchange capacity on XA-9, which is expected to keep more OH^- at the catalyst surface and improve local pH, thereby leading to a lower H_2 FE and a higher C_2H_4 FE. While at the higher current density (>700 mA cm^{-2}), the PFSA showed better performance of C_2H_4 production and HER suppression. The PFSA allows cation (e.g., H^+ and K^+) transport from the electrolyte to catalyst surface while slowing OH^- diffusion out. It would lead to a higher surface pH to facilitate C-C coupling under a high current density.

We prepared the control sample with flipped CoPc@HC and Cu geometry, denoted as Cu/CoPc@HC. The performance of Cu/CoPc@HC is inferior compared to the proposed tandem architecture - CoPc@HC/Cu (Supplementary Fig. 27).

We also investigated the effect of the loading of catalyst layers on performance. The observed trends in C_{2+} and CO FE depend on the rate of CO generation and the degree of CO utilization. Due to limited active surface of sputtered Cu, the CoPc@HC catalyst layer of CoPc@HC/sCu can produce enough CO to ensure a high CO availability on the Cu surface at low current densities, which can suppress HER and promote C-C coupling to produce C_{2+}. When the thicker Cu layer is introduced to capture CO from the CoPc@HC catalyst layer, the amount of CO distributed on the surface of Cu nanoparticles is insufficient in low current densities, leading to a limited effect in suppressing HER and facilitating the C-C coupling for C_{2+} production. As the increase of current densities, more CO is produced by CoPc@HC catalyst layer, which enhances the local CO concentration of the Cu surface. This enables

CoPc@HC/Cu electrode to facilitate C-C coupling for higher C_{2+} FE and suppress HER for a lower H_2 FE at high current densities. We further prepared the tandem electrodes with different thicknesses (Supplementary Fig. 28). When the loading of the ionomer-modified Cu nanoparticle layer was reduced from 1 mg cm^{-2} to 0.5 mg cm^{-2}, the CoPc@$HC_{0.5}$/$Cu_{0.5}$ electrode exhibits a higher C_{2+} FE and a lower H_2 FE at a lower current density compared with CoPc@$HC_{0.5}$/Cu_1 electrode. This result is attributed to a higher local CO concentration on the Cu surface. On the other hand, the lower loading of the ionomer-modified Cu layer means lower Cu active sites that capture and activate the CO in a high current density, which leads to a higher CO FE and a lower C_{2+} FE. The performance results confirm that the CoPc@$HC_{0.5}$/$Cu_{0.5}$ electrode achieved a peak C_{2+} FE of 69%, which is lower than that of the CoPc@HC/Cu electrode with a peak C_{2+} FE of 80%. When the loading of CoPc@HC catalyst layer was increased from 0.5 mg cm^{-2} to 1 mg cm^{-2}, the CoPc@HC_1/Cu_1 electrode exhibits a higher C_{2+} FE and a lower H_2 FE at a lower current density compared with CoPc@HC/Cu electrode compared with CoPc@HC/Cu electrode. And CoPc@HC_1/Cu_1 electrode achieves a highest C_{2+} FE of 83% and a lowest H_2 FE of 7.7% at 900 mA cm^{-2}, which is better than CoPc@$HC_{0.5}$/Cu_1. These results are ascribed to a higher CO concentration on the Cu surface because a higher loading of CoPc@HC layer can provide more CO to spill over to the Cu surface. This is also supported by a higher CO FE on CoPc@HC_1/Cu_1 electrode compared with CoPc@$HC_{0.5}$/Cu_1.

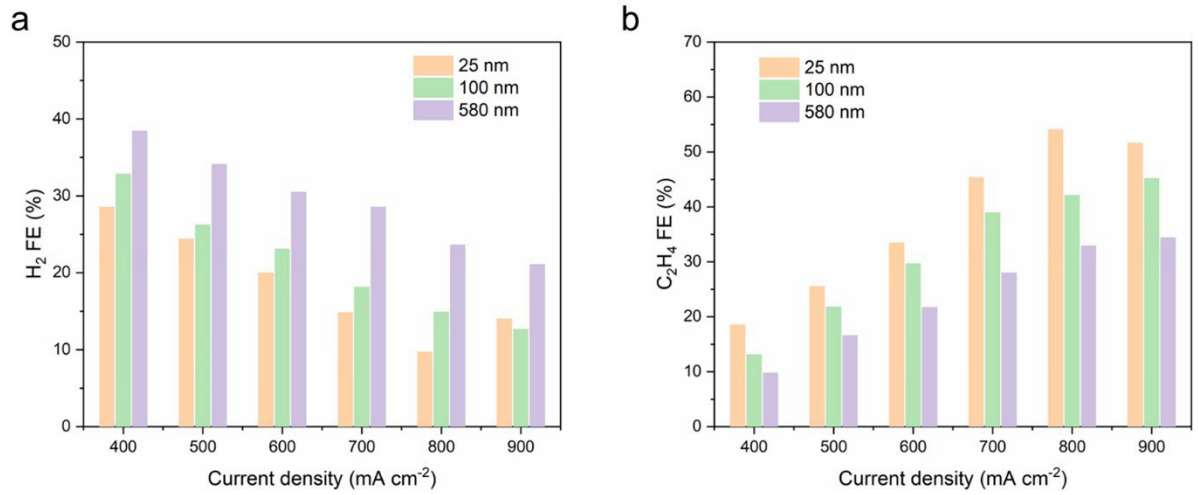

Supplementary Figure 25 | a-b, Comparison of FEs of H_2 (**a**) and C_2H_4 (**b**) on CoPc@HC/Cu electrodes with different sizes of Cu nanoparticles in Cu catalyst layers in an acidic buffer electrolyte of 0.5 M H_3PO_4 and 0.5 M KH_2PO_4 with 2.5 M KCl in flow cell. The testing temperature is 25 ℃.

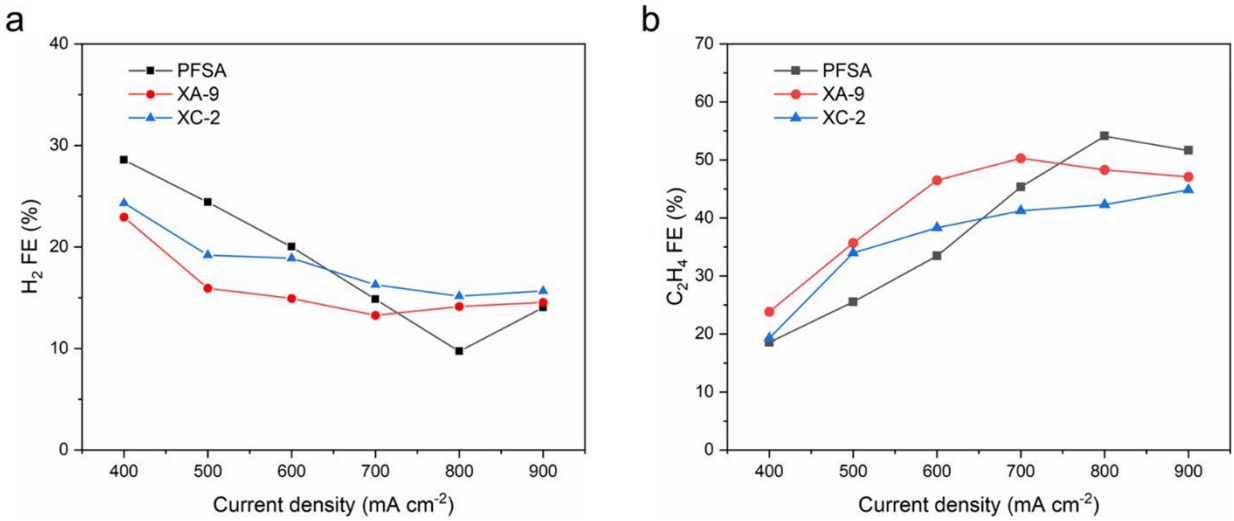

Supplementary Figure 26 | a-b, Comparison of FEs of H_2 (**a**) and C_2H_4 (**b**) on CoPc@HC/Cu electrodes with different ionomers in Cu catalyst layers in an acidic buffer electrolyte of 0.5 M H_3PO_4 and 0.5 M KH_2PO_4 with 2.5 M KCl in flow cell. The testing temperature is 25 ℃.

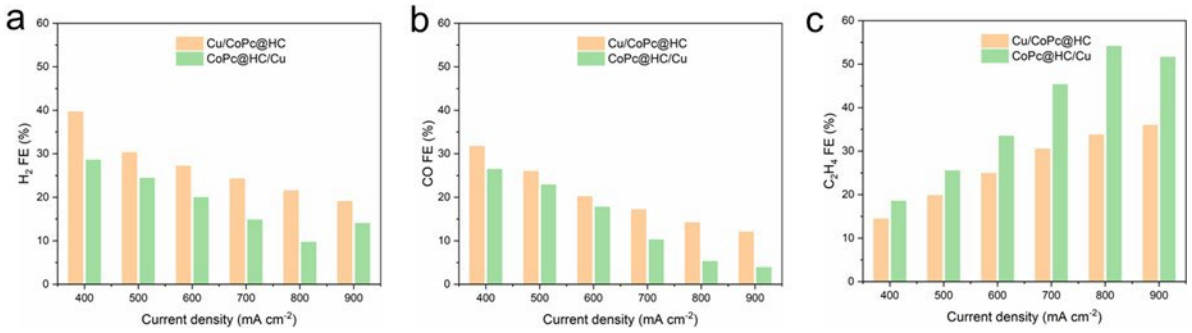

Supplementary Figure 27 | a-c, Comparison of FEs of H_2 (**a**), CO (**b**) and C_2H_4 (**c**) on CoPc@HC/Cu and Cu/CoPc@HC electrodes in in an acidic buffer electrolyte of 0.5 M H_3PO_4 and 0.5 M KH_2PO_4 with 2.5 M KCl in flow cell. Cu/CoPc@HC is the control sample with flipped CoPc@HC and Cu geometry. The testing temperature is 25 ℃.

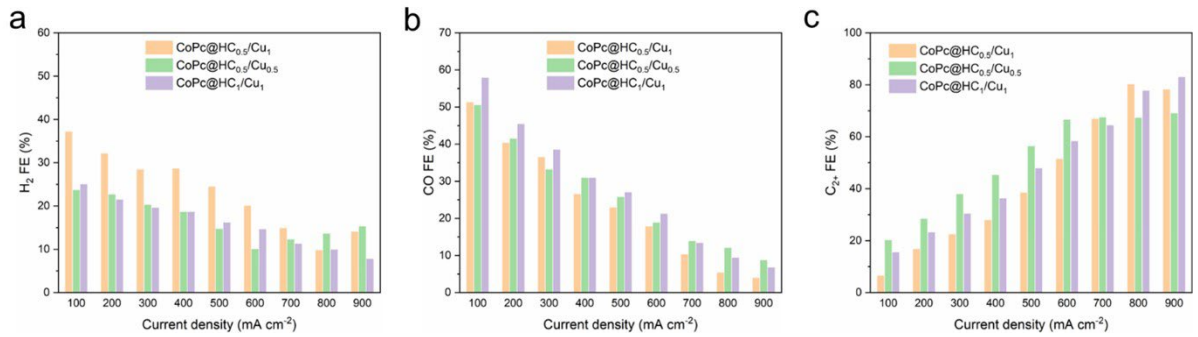

Supplementary Figure 28 | a-c. Comparison of FEs of H_2 (**a**), CO (**b**) and C_{2+} (**c**) on CoPc@HC/Cu tandem electrode with different loadings of CoPc@HC and Cu catalyst layers. CoPc@$HC_{0.5}$/Cu_1 (CoPc@HC/Cu) represents that the loading of CoPc@HC catalyst layer is 0.5 mg cm^{-2} and the loading of the ionomer-modified Cu catalyst layer is 1 mg cm^{-2}. CoPc@$HC_{0.5}$/$Cu_{0.5}$ represents that the loading of CoPc@HC catalyst layer is 0.5 mg cm^{-2} and the loading of the ionomer-modified Cu catalyst layer is 0.5 mg cm^{-2}. CoPc@HC_1/Cu_1 represents that the loading of the CoPc@HC catalyst layer is 1 mg cm^{-2} and the loading of the ionomer-modified Cu catalyst layer is 1 mg cm^{-2}. The testing temperature is 25 ℃.

Supplementary Note 4 | The effect of electrolytes on acidic CO_2RR performance.

To investigate the contribution of Cl^- to C_2H_4 formation in acidic conditions, we conducted some control experiments. Firstly, we varied the concentration of KCl in the electrolyte to 0.5 M, 1.5 M, and 2.5 M. As shown in Supplementary Fig. 29a, the C_2H_4 FE on CoPc@HC/Cu electrode improved as the KCl concentration increased. It is noted that the K^+ concentration also varied, and K^+ has been demonstrated to play a critical role in acidic CO_2RR systems. Therefore, we attempted to fix the K^+ concentration and vary the anion in the catholyte. Due to the limited solubility of other potassium salts, we fixed the K^+ concentration with 0.5 M for a fair comparison. Excluding reducible anions (NO_3^- and ClO_4^-) and anions that are unstable in acidic conditions (CO_3^-, HCO_3^- and I^-), Br^- and SO_4^{2-} were selected as control samples. As shown in Supplementary Fig. 29b, compared with 0.5 M KBr and saturated K_2SO_4 (slightly less than 0.25 M), CoPc@HC/Cu electrode exhibited a slightly highest C_2H_4 FE with 0.5 M KCl as an additive under the same current densities. We also compared saturated KBr (slightly less than 2.5 M) and 2.5 M KCl, the result showed CoPc@HC/Cu electrode exhibited a slightly higher C_2H_4 FE with 2.5 M KCl as an additive (Supplementary Fig. 29c). The results suggested that Cl^- provides a slight enhancement in C_2H_4 production, albeit to a limited extent. Therefore, considering the solubility and performance enhancement, we chose 2.5 M KCl as an additive into an acidic buffer electrolyte of 0.5 M H_3PO_4 and 0.5 M KH_2PO_4.

We also evaluated the performance of CoPc@HC/Cu tandem electrode in different acidic electrolytes (Supplementary Fig. 30), which showed CoPc@HC/Cu electrode exhibit a higher ethylene FE and C_{2+} FE as well as a lower H_2 FE at a lower current density in non-buffered sulfuric acid electrolyte compared with buffer phosphoric acid electrolyte. This result can be attributed to the higher local pH attained on the catalyst surface in sulfuric acid electrolyte, since sulfuric acid lacks buffering capacity unlike phosphoric acid.

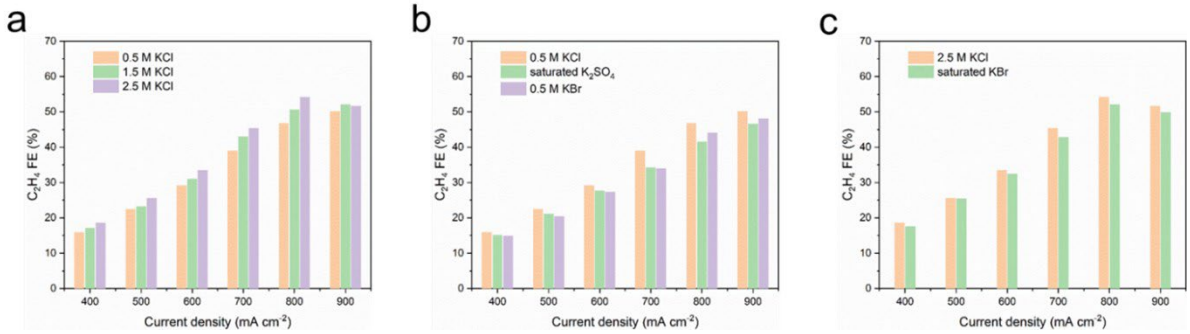

Supplementary Figure 29 | C_2H_4 FE on CoPc@HC/Cu electrode in acidic CO_2RR in an acidic buffer electrolyte of 0.5 M H_3PO_4 and 0.5 M KH_2PO_4 with different K salt additives. a, C_2H_4 FE on CoPc@HC/Cu in different KCl concentrations. **b**, C_2H_4 FE on CoPc@HC/Cu in 0.5 M KCl, saturated K_2SO_4 (slightly less than 0.25 M) and 0.5 M KBr. **c**, C_2H_4 FE on CoPc@HC/Cu in 2.5 M KCl and saturated KBr (slightly less than 2.5 M). The testing temperature is 25 ℃.

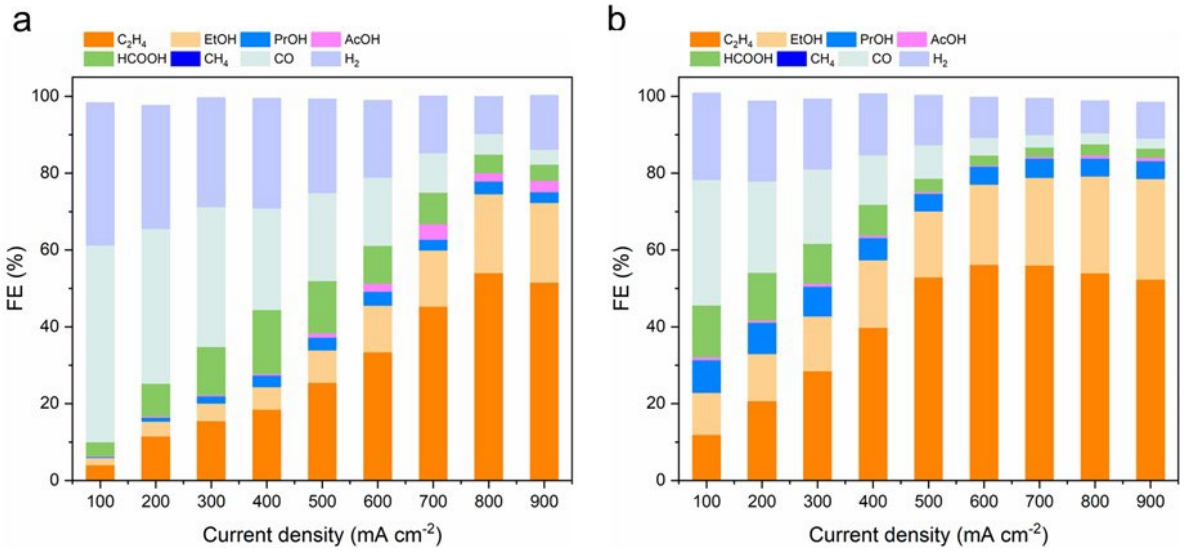

Supplementary Figure 30 | Comparison of FEs of CO_2RR products on CoPc@HC/Cu tandem electrode in the buffered and non-buffered acidic electrolytes in flow cell. a, FEs of CO_2RR products on CoPc@HC/Cu tandem electrode in an acidic buffer electrolyte of 0.5 M H_3PO_4 and 0.5 M KH_2PO_4 with 2.5 M KCl. **b**, FEs of CO_2RR products on CoPc@HC/Cu tandem electrode in a non-buffer acidic electrolyte of 0.05 M H_2SO_4 with 2.5 M KCl. The testing temperature is 25 ℃.

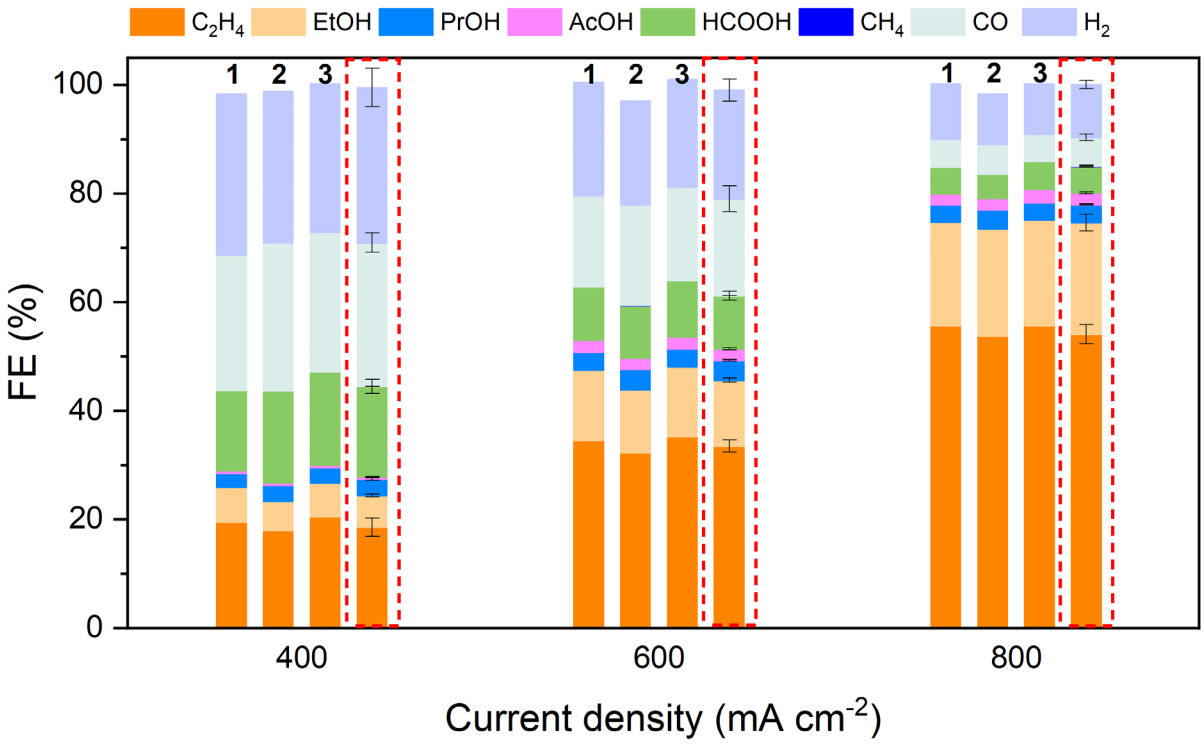

Supplementary Figure 31 | Additional three independent experiments for electrode preparation and performance assessment of CoPc@HC/Cu tandem electrode in 0.5 M H_3PO_4 and 0.5 M KH_2PO_4 with 2.5 M KCl in a flow cell with a CO_2 flow rate of 10 ml min^{-1}. For comparison, the performance of the original CoPc@HC/Cu tandem electrodes is showed inside the red dashed box. Values are means, and error bars represent the standard deviation from three independent measurements. The acidic CO_2RR performance was consistently achieved on CoPc@HC/Cu tandem electrode, suggesting a good reproducibility. The testing temperature is 25 ℃.

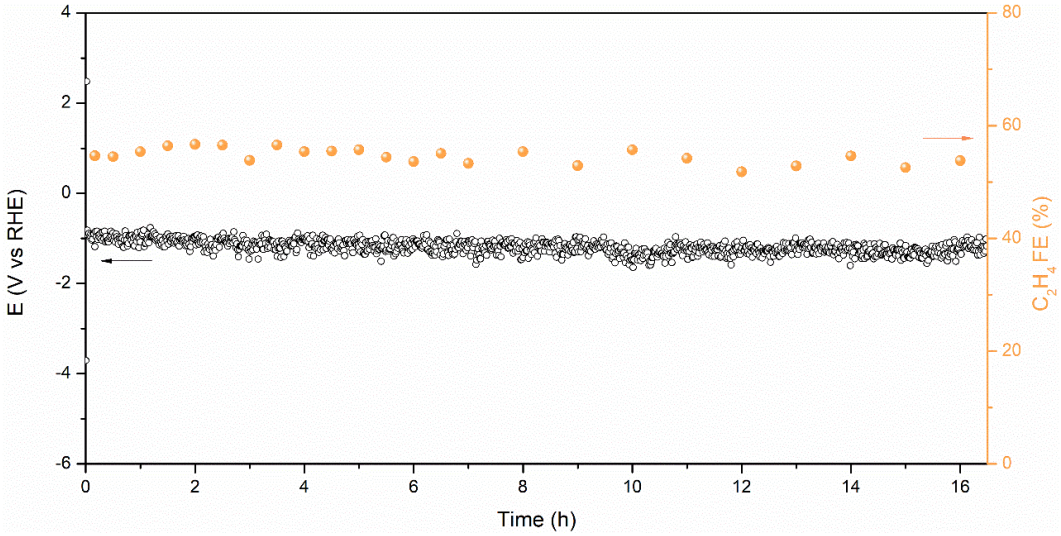

Supplementary Figure 32 | The stability of CoPc@HC/Cu electrode at the current density of 800 mA cm^{-2}, which shows CoPc@HC/Cu electrode maintains the stable potential and C_2H_4 FE for 16 h. The testing temperature is 25 ℃.

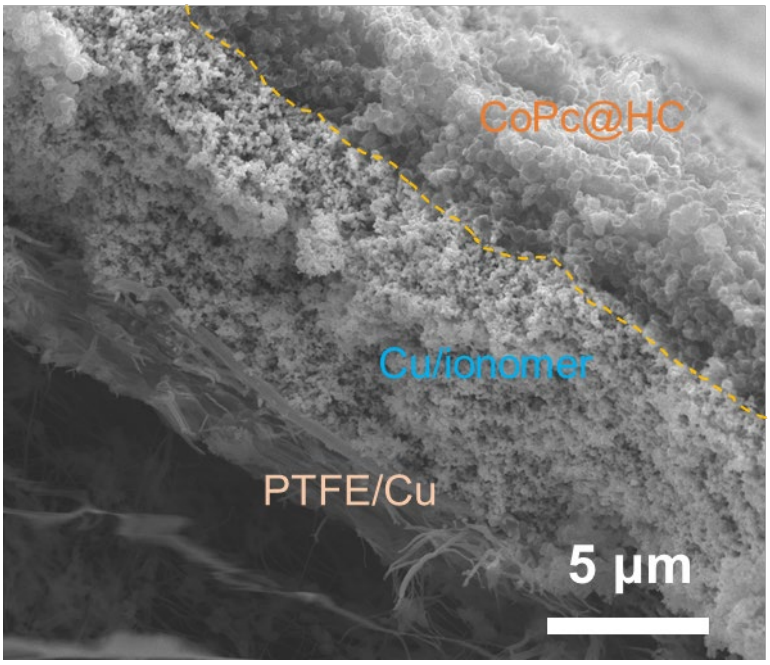

Supplementary Figure 33 | The cross-sectional SEM image of the used CoPc@HC/Cu electrode after the stability test.

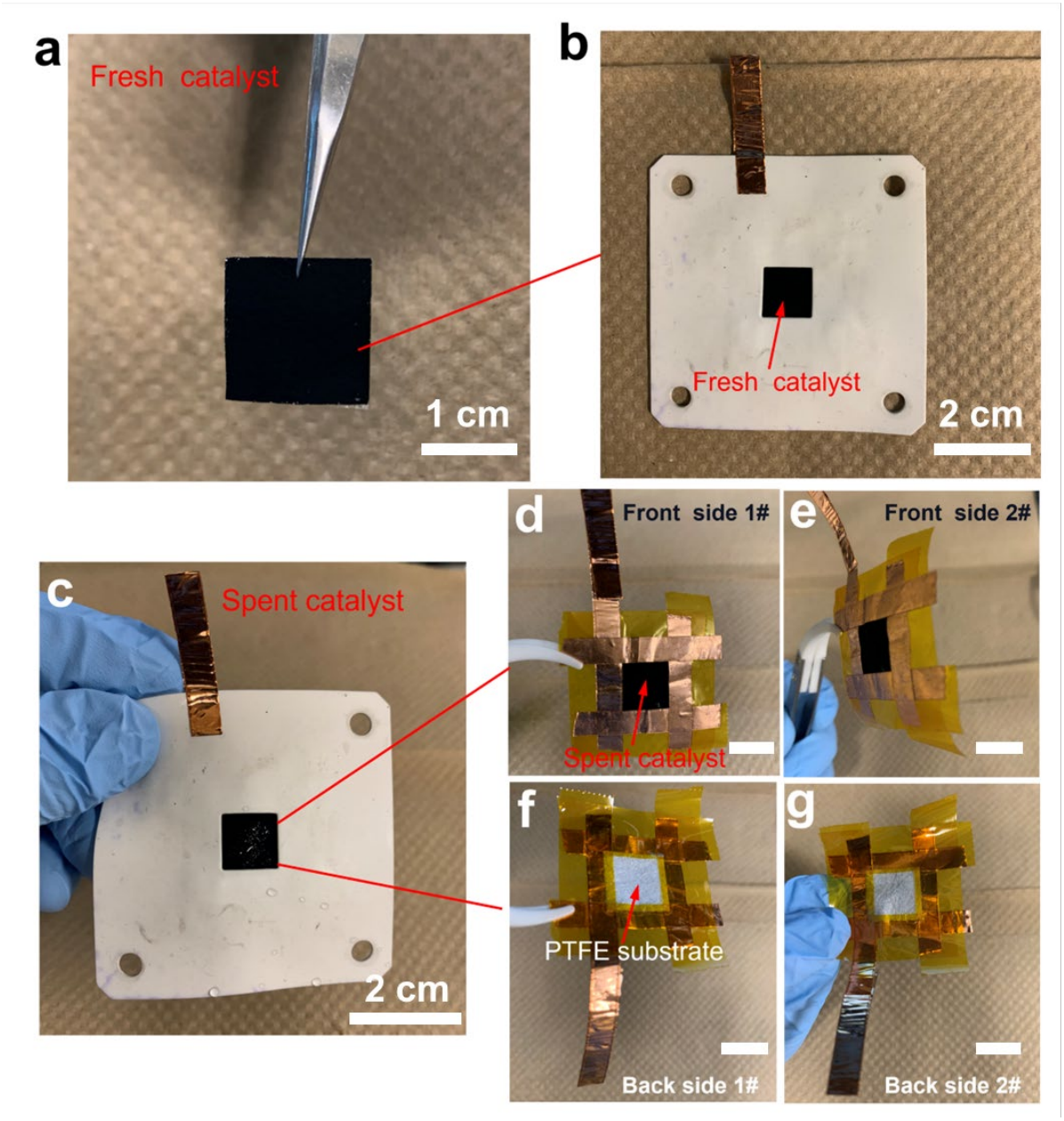

Supplementary Figure 34 | a-b, The pictures of the fresh CoPc@HC/Cu electrode. **c-g**, the pictures of the used CoPc@HC/Cu electrode after stability test. Scale bar in **d-g** is 1 cm. The CoPc@HC/Cu electrode remains intact on PTFE without peeling off, suggesting a good mechanical stability.

Supplementary Note 5 | The two-layered tandem electrode configuration

We design and deploy two separately optimized distinct catalyst layers in tandem to form a two-layered tandem electrode for the efficient transformation of CO_2-to-C_{2+}. The two-layer tandem electrode configuration enables the formation of an elevated interfacial CO concentration along the boundary of CoPc@HC and Cu catalyst layers, which is attributed to the substantial and collective orientation of CoPc@HC. The continuous migration of CO molecules towards the Cu layer, resulting in a high CO flux, is prompted by hydraulic pressure and the low aqueous solubility of CO gas (Supplementary Fig. 35 and Supplementary Fig. 36a). The high CO flux in the two-layer tandem electrode configuration augments the interfacial CO concentration, which creates a CO-rich environment for the second Cu catalyst layer. This is beneficial in suppressing H adsorption on the Cu surface in bulk acidic conditions, thereby keeping H_2 FE below 10%. In contrast, in the mixed-one-layer tandem electrode configuration, the CoPc@HC catalyst is dispersed alongside Cu catalyst. This distribution leads to a significant reduction in the interfacial CO concentration between Cu and CoPc@HC (Supplementary Fig. 36b). This decreased interfacial CO concentration proves less effective in suppressing the H adsorption under the acidic bulk environment, leading to a higher H_2 FE and lower C_{2+} FE (Supplementary Figs. 35-38). Therefore, the two-layered tandem electrode configuration is beneficial to performance enhancement in acidic CO_2RR.

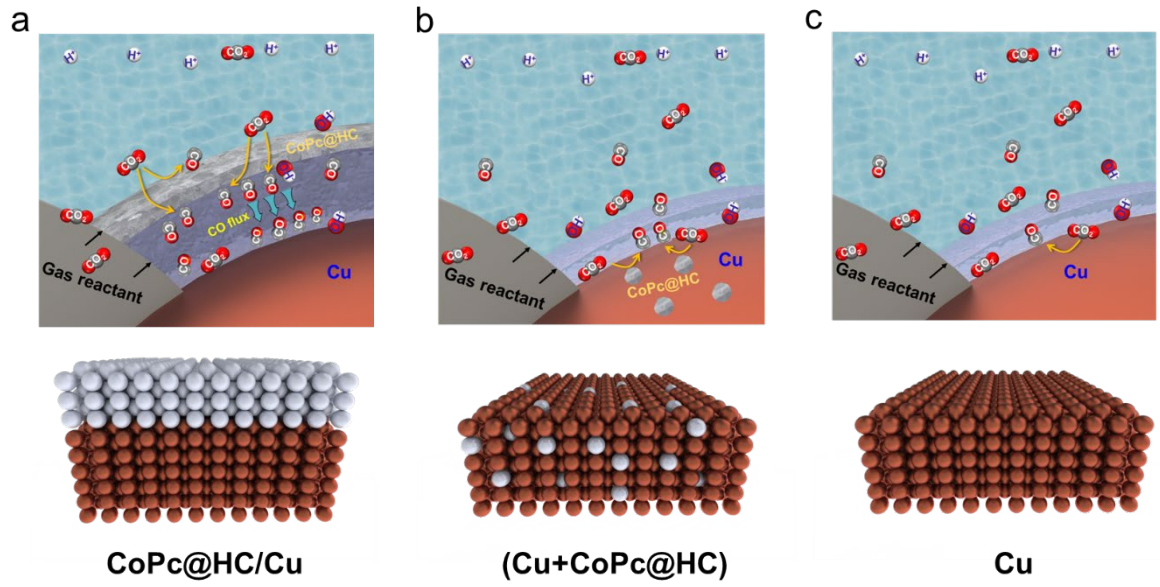

Supplementary Figure 35 | a, The schematic of local reaction environment of CoPc@HC/Cu tandem electrode. The schematic illustrates a high CO flux is generated to create a CO-rich environment to suppress HER and promote C-C coupling for ensuing C_{2+} production formation on the Cu catalyst layer. **b**, The schematic of local reaction environment of mixed one-layer tandem (Cu+CoPc@HC) electrode. **c**, The schematic of local reaction environment of Cu electrode.

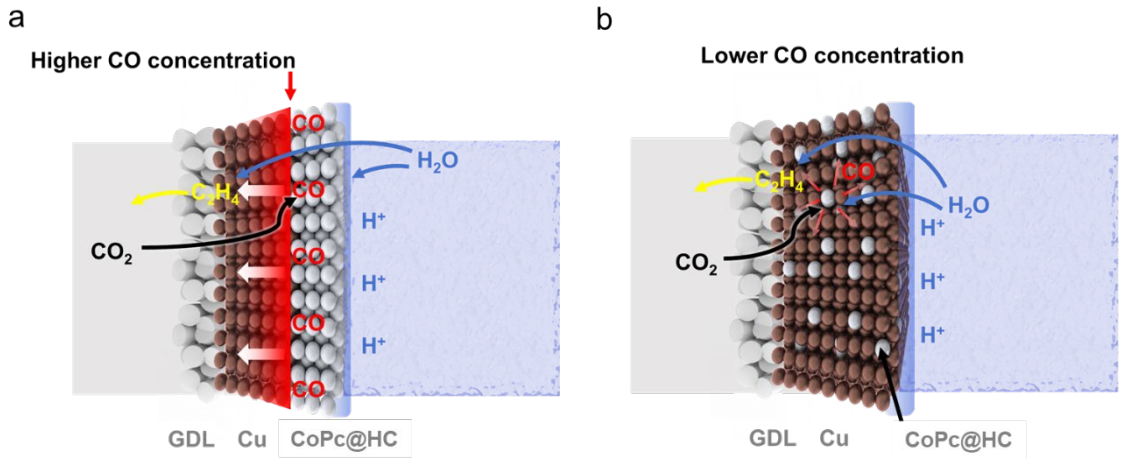

Supplementary Figure 36 | a, The schematic illustrates a two-layer tandem electrode configuration that enables the formation of an elevated interfacial CO concentration along the boundary of CoPc@HC and Cu. **b**, The schematic illustrates a mixed-one-layer tandem electrode configuration. The CoPc@HC catalyst is dispersed alongside the Cu catalyst. This distribution leads to a significant reduction in the interfacial CO concentration between Cu and CoPc@HC.

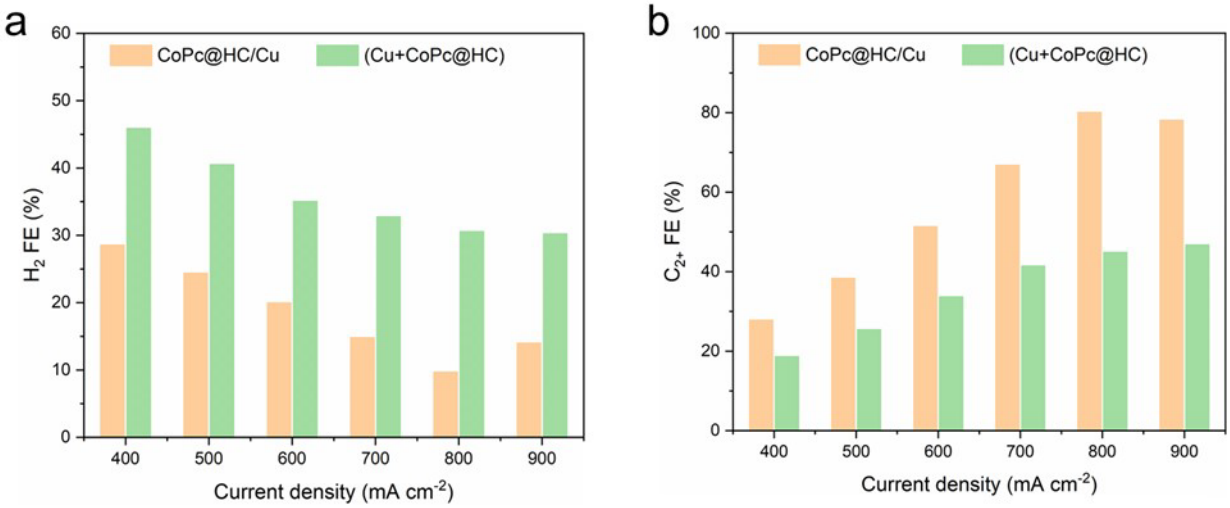

Supplementary Figure 37 | a-b, Comparison of FEs of H_2 (**a**) and C_{2+} (**b**) on our two-layered tandem CoPc@HC/Cu electrode and the mixed one-layer tandem electrode (Cu+CoPc@HC) electrode in in an acidic buffer electrolyte of 0.5 M H_3PO_4 and 0.5 M KH_2PO_4 with 2.5 M KCl in flow cell. The testing temperature is 25 ℃.

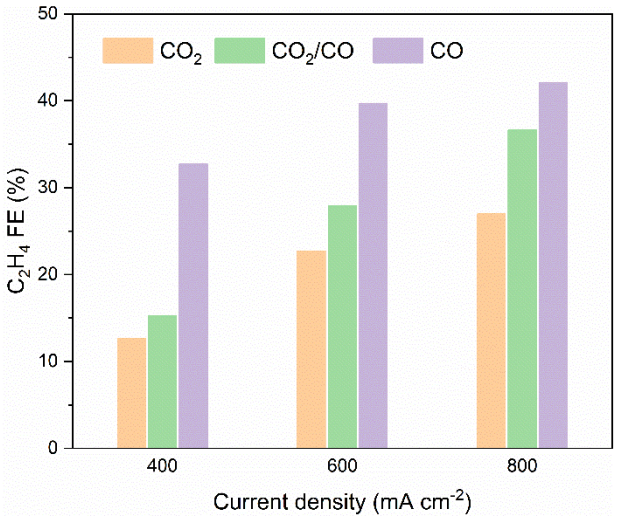

Supplementary Figure 38 | C_2H_4 FE on the Cu in an acidic buffer electrolyte of 0.5 M H_3PO_4 and 0.5 M KH_2PO_4 with 2.5 M KCl in CO_2 feed, CO_2/CO internal co-feed, and CO feed. The mixed-one-layer (Cu+CoPc@HC) tandem electrode generates an internal CO_2/CO co-feed condition, as the CoPc@HC acts as a selective CO producer. The testing temperature is 25 ℃.

Supplementary Note 6 | COMSOL simulation.

We performed the COMSOL simulation to simulate the local pH (Supplementary Fig. 39). All the interaction between species in the electrolyte (CO_2, HCO_3^-, CO_3^{2-}, H_3PO_4, $H_2PO_4^-$, HPO_4^{2-}, PO_4^{3-}, OH^-, H^+ and H_2O) were considered. Modeling of reaction and diffusion of species within a typical diffusion layer of 10 μm indicates that in the phosphoric acid buffer electrolyte, the surface (distance to the cathode of 0 μm) pH slightly increases to become alkaline as the increase of current density. The locally alkaline conditions result from a consumption rate of local protons that exceeds the mass transport of protons from the bulk. Despite elevated pH at the surface, pH decreases to an acidic range within a short distance of the cathode. Even at a current density as high as 900 mA/cm^2, the pH decreases to 6.3 [first acid dissociation constant (pK_{a1}) of carbonic acid] within 5 μm of the electrode. This result suggests that any locally formed carbonate would be converted back to CO_2 for ensuing reduction, avoiding carbonate crossover. We also investigated the pH distribution in the non-buffered sulfuric acid electrolyte (Supplementary Fig. 40). In the same position of the diffusion layer, the pH values in the non-buffered sulfuric acid are higher than those in the buffered phosphoric acid, indicating a higher local pH in the catalyst surface can be reached at a lower current density in the non-buffered sulfuric acid electrolyte compared with the buffered phosphoric acid electrolyte. This suggests that catalysts exhibit a higher ethylene FE and C_{2+} FE in a lower current density in the non-buffered sulfuric acid electrolyte. This finding is consistent with the experimental results (Supplementary Fig. 30).

1D COMSOL Multiphysics Model:

The one-dimensional electrochemical reaction profile modelled by COMSOL Multiphysics version 5.5. This study aimed to further understand and compare the local pH profile between the acidic buffer electrolyte condition (0.5M H_3PO_4/0.5M KH_2PO_4 with 2.5M KCl) and the non-buffer acidic electrolyte condition (0.05M H_2SO_4 with 2.5 KCl). The Electrostatics (es), Secondary Current Distribution (cd), and Transport of Diluted Species (tds) were used to model the interactions between H_3PO_4, $H_2PO_4^-$, HPO_4^{2-}, PO_4^{3-}, CO_2, HCO_3^-, CO_3^{2-}, H^+, OH^-, and K+ in a stationary study. The detailed geometry of the simulation includes a copper cathode catalyst layer, an electric double layer, and a 10-μm thick diffusion layer. At the left-

hand boundary of the catalyst layer, the initial aqueous CO_2 concentration was set, while a bulk equilibrium concentration of acidic buffer electrolyte/acidic electrolyte was set at the right-hand boundary of the diffusion layer. An electrical potential was applied at the left-hand boundary of the catalyst layer and the ground was set at the right-hand boundary of the diffusion layer. Two general assumptions were made for this study. Firstly, an electrolyte was distributed evenly through the diffusion domain. Secondary, the applied current was evenly distributed within the catalyst surface.

Detailed COMSOL Physics Setup:

Henry's Law and Sechenov equations (E1-E3) were applied to determine the CO_2 solubility in an aqueous solution. The CO_2 was assumed to be an ideal gas, and the aqueous CO_2 concentration was governed by pressure, temperature, and salinity [3-5].

$C_{CO_2(aq)} = P_{CO_2} \times K_s \times K^0_{H,CO_2}$	(E1)
$K_s = 10^{-c_K(0.0922+h_{G,0})-c_{OH}(0.0839+h_{G,0})-c_{CO3}(0.1423+h_{G,0})-c_{Hco3}(0.0967+h_{G,0})}$	(E2)
$ln\left(K^0_{H,CO_2}\right) = 93.4517 \times \frac{100}{T} - 60.2409 + 23.3585 \times ln\left(\frac{T}{100}\right)$	(E3)

Where $C_{CO_2(aq)}$ represents the initial aqueous CO_2 concentration applied at the boundary of the Cu catalyst layer. P_{CO_2} is the partial pressure of CO_2 in the inlet stream using a value of 1, Sechenov constant (K_s) and Henry's Law constant of CO_2 (K^0_{H,CO_2}) were calculated based on local concentrations and reaction environments. The $h_{G,0}$ is calculated using a value of -0.0172 for CO_2. The input temperature (T) is calculated using room temperature of 300 K.

The simulation utilized the combination of electrolyte potential (ϕ) and electroneutrality (ψ) to simulate the electromigration of different charged species (E4). The porous Cu catalyst domain was assumed to consist of 40% electrode volume fraction with electrical conductivity of $0.8*10^5$ S/m and 60% electrolyte volume fraction with electrical conductivity of 4.56 S/m, as the same manner reported in the previous study [6]. The application of Ohm's Law (E5) was applied for the calculation of electrical potential. The Poisson equation (E6) was applied to maintain electroneutrality and determined the induced space charge.

$V = \phi + \psi$	(E4)
$i = -\sigma \frac{\partial \phi}{\partial x}$	(E5)
$\nabla \times (\varepsilon_0 \varepsilon_r \nabla \phi(r)) = -F \sum_i z_i C_i$	(E6)

Where ε_0 is the permittivity of vacuum (8.854×10^{-12} F/m), ε_r is the relative permittivity of water (80), F represents the Faraday constant (96485), and z_i is the charge number, shown in Supplementary Table 3. The Poisson equation was used to solve C_i and $\phi(r)$ numerically.

The Poisson-Nernst-Planck set of equations (E7, E8) were applied for species transport, the combination of diffusion and electromigration were considered. The Millington and Quirk set of equation (E9, E10) were used to calculate the porous domain effective diffusivity. The porosity value of 0.6 was assumed for the Cu catalyst layer, in line with a previous study [7].

$\frac{\partial c_i}{\partial t} + \frac{\partial J_i}{\partial x} = \Sigma R_i$	(E7)
$J_i = -\frac{D_i \partial c_i}{\partial x} - \frac{z_i D_i}{RT} F c_i \frac{\partial V}{\partial x}$	(E8)
$D_i = \frac{\epsilon_p}{\tau_{F,i}} D_{F,i}$	(E9)
$\tau_{F,i} = \epsilon_p^{-1/3}$	(E10)

R_i, c_i, D_i, $D_{F,i,}$ ϵ_p, $\tau_{F,i}$, J_i, R, $and\ T$ represent the electrochemical reaction rate, species concentration, effective diffusion coefficient, bulk diffusion coefficient, porosity coefficient (0.9), tortuosity coefficient, flux of species, ideal gas constant (8.314 J mol^{-1} K^{-1}), operation temperature (room temperature of 300 K), respectively. The bulk diffusion coefficient was obtained from the literature, as shown in Supplementary Table 3.

Supplementary Table 3. Diffusion coefficient and charge number for different species [8-11].

Species	$D_{F,i}$ [m^2s^{-1}]	Z_i [-]
CO_2	1.91×10^{-9}	0
CO_3^{2-}	0.923×10^{-9}	-2
HCO_3^-	1.185×10^{-9}	-1
H^+	9.31×10^{-9}	+1
OH^-	5.273×10^{-9}	-1
H_3PO_4	0.918×10^{-9}	0
$H_2PO_4^-$	0.918×10^{-9}	-1
HPO_4^{2-}	0.458×10^{-9}	-2
PO_4^{3-}	0.612×10^{-9}	-3

The CO_2 reaction rate and hydroxide generation rate were calculated using Faraday's electrochemical reaction equations for a range of current densities from 100 to 900 mA cm^{-2} (E11, E12). The Faradic efficiency of each product was determined based on experimental results.

$r_{CO_2} = -\frac{i}{F} * \left(\frac{FE_{HCOOH}}{2} + \frac{FE_{CO}}{2} + \frac{FE_{CH4}}{8} + \frac{FE_{CH3COOH}}{8} + \frac{FE_{C2H4}}{12} + \frac{FE_{C2H5OH}}{12}\right)$	(E11)
$r_{OH^-} = \frac{i}{F}$	(E12)

The carbonate equilibria (E13, E14) and water dissociation (E15) were considered for all domains and the forward and reverse reaction rate constants were determined as the same manner as previous studies [12,13].

$CO_2(aq) + OH^- \leftrightarrow HCO_3^-$	(E13)
$HCO_3^- + OH^- \leftrightarrow CO_3^{2-} + H_2O$	(E14)
$H_2O \leftrightarrow H^+ + OH^-$	(E15)

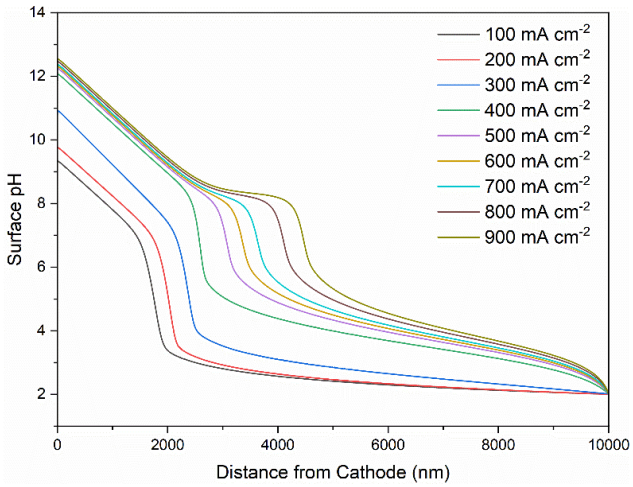

Supplementary Figure 39 | Modelling of pH changes along the catalyst surface in an acidic buffer electrolyte of 0.5 M H_3PO_4 and 0.5 M KH_2PO_4 with 2.5 M KCl under different applied current densities.

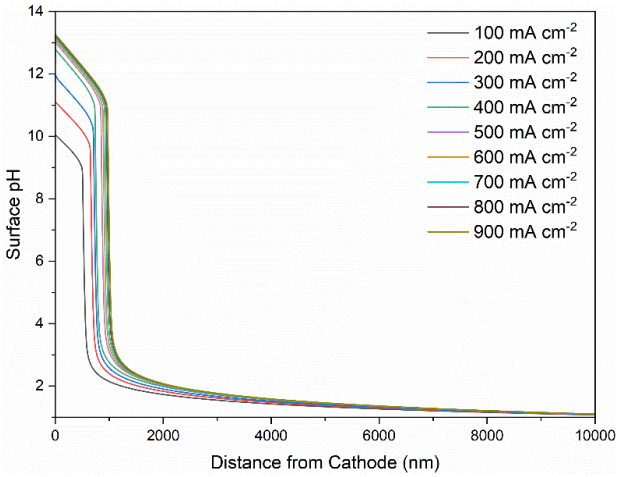

Supplementary Figure 40 | Modelling of pH changes along the catalyst surface in a non-buffer acidic electrolyte of 0.05 M H_2SO_4 with 2.5 M KCl under different applied current densities.

Supplementary Note 7 | Single pass conversion efficiency (SPCE) measurement.

We also pursued a high single-pass carbon efficiency (SPCE) using the tandem electrode to reduce the energy penalty associated with the cathodic gas separation of unreacted CO_2 and product separation from dilute streams. Reducing the flow rate of CO_2 to 2 standard cubic centimeters per minute (sccm), we obtained a maximum SPCE of 87% for all the CO_2RR products (Fig. 3h). For comparison, the SPCE on the Cu electrode is 52%, when the system is supplied with the same flow rate of CO_2 (Supplementary Fig. 41), indicating higher SPCE can benefit from our decoupled strategy. In acidic CO_2RR, CO_2 lost to carbonate formation is recovered by reacting with protons in the bulk electrolyte. In addition to this recovery mechanism, the CoPc@HC/Cu tandem electrode offers an avenue to rapidly convert CO_2 into CO, which does not transform into carbonates in local alkaline conditions (Fig. 1e). Our spatially decoupled strategy enables the remarkable enhancement on the SPCE from 52% to 87% when the CoPc@HC/Cu tandem electrode was implemented (Supplementary Fig. 42). When further optimized for single-pass utilization, this CoPc@HC/Cu achieves an SPCE of 91% at 800 mA cm^{-2} (Supplementary Fig. 43).

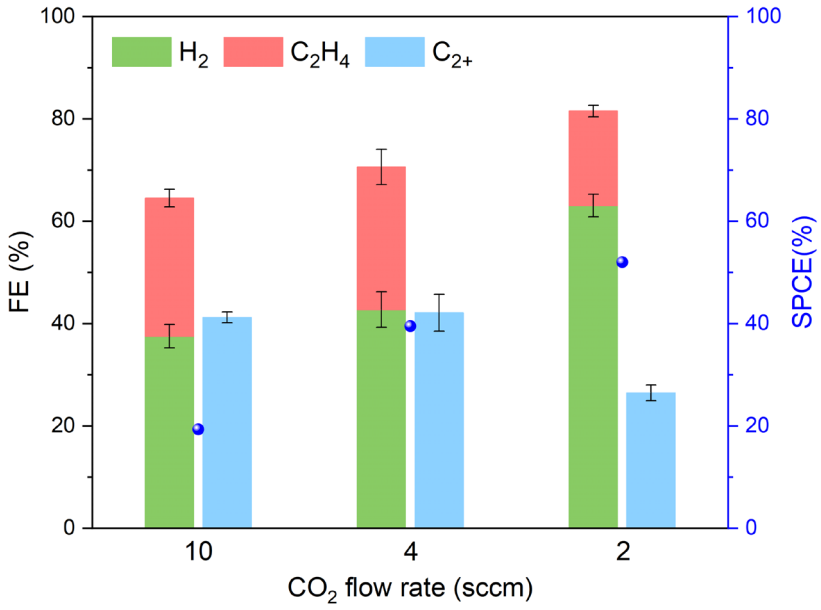

Supplementary Figure 41 | FEs of CO_2RR products and SPCE on Cu electrode at 800 mA cm^{-2} with different flow rates of CO_2 inlet in the acidic buffer electrolyte of 0.5 M H_3PO_4 and 0.5 M KH_2PO_4 with 2.5 M KCl. Values are means, and error bars represent the standard deviation from three independent measurements (n=3). The testing temperature is 25 ℃.

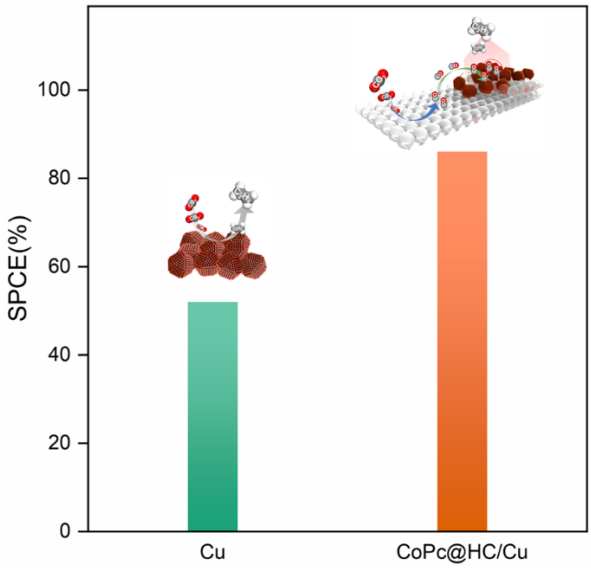

Supplementary Figure 42 | SPCE on CoPc@HC/Cu electrode and Cu electrode at 800 mA cm^{-2} in CO_2 inlet flow rate of 2 sccm in the acidic buffer electrolyte of 0.5 M H_3PO_4 and 0.5 M KH_2PO_4 with 2.5 M KCl in flow cell. The testing temperature is 25 ℃.

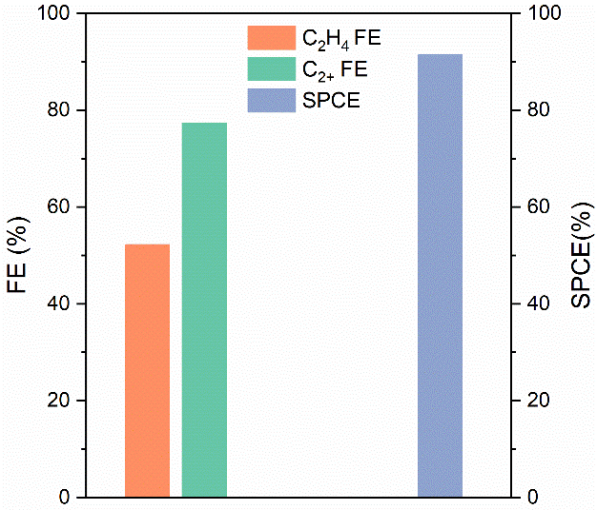

Supplementary Figure 43 | FEs of C_2H_4 and C_{2+} products and SPCE with CO_2 feed rate of 10 ml min^{-1} at the applied current density of 800 mA cm^{-2} in a 5 cm^2 electrolyzer in the acidic buffer electrolyte of 0.5 M H_3PO_4 and 0.5 M KH_2PO_4 with 2.5 M KCl in flow cell. The testing temperature is 25 ℃.

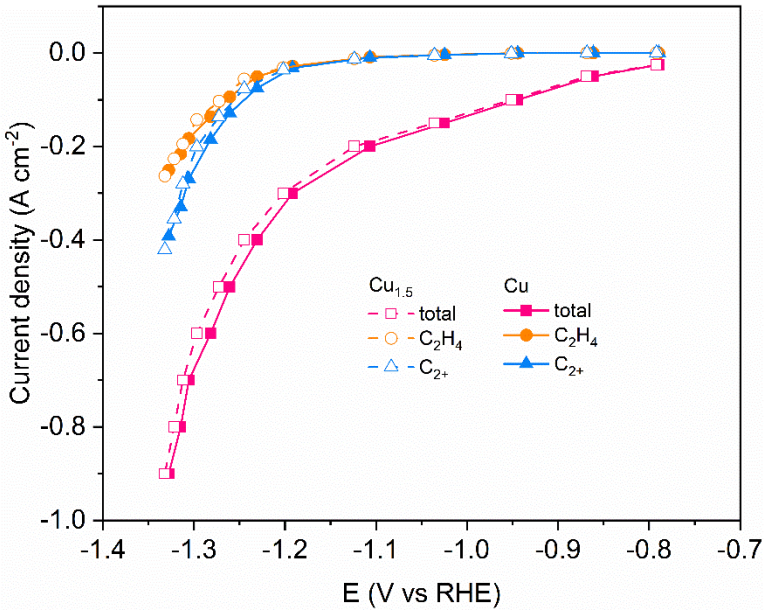

Supplementary Figure 44 | Current density-potential curve toward CO_2RR products on Cu electrodes with Cu loading of 1 mg cm (Cu) and 1.5 mg cm^{-2} ($Cu_{1.5}$). The testing temperature is 25 °C.

In our tandem system, the Cu loading is 1 mg cm^{-2} and CoPc@HC loading is 0.5 mg cm^{-2}. To exclude the influence of catalyst loading, we prepared a Cu electrode with a loading of 1.5 mg cm^{-2} as a control sample. Supplementary Fig. 41 shows that the Cu electrode with a loading of 1.5 mg cm^{-2} exhibits a similar current density-potential curve with that of the Cu electrode with a loading of 1 mg cm^{-2}, and the selectivities of ethylene and C_{2+} are also comparable. To ensure a fair comparison, we have added the comparison of the current density-potential curve toward CO_2RR products on CoPc@HC/Cu tandem electrode and $Cu_{1.5}$ electrode in Supplementary Fig. 42.

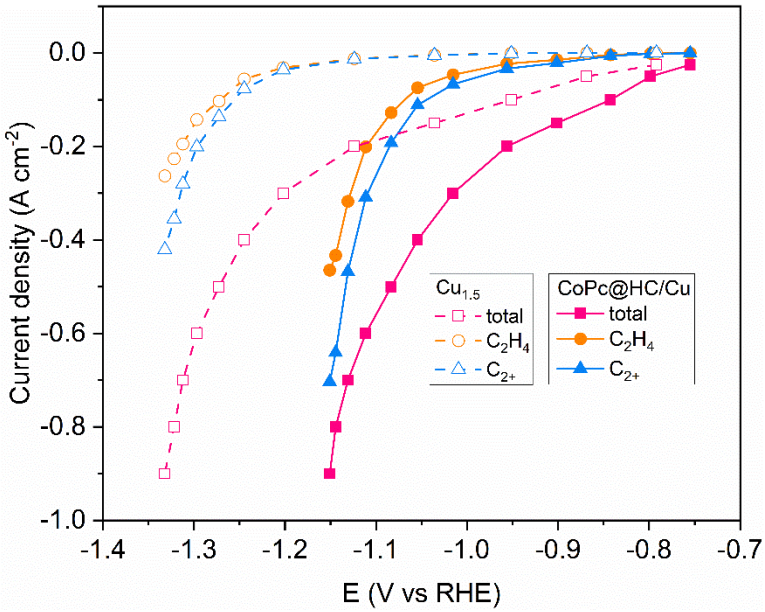

Supplementary Figure 45 | Current density-potential curve toward CO_2RR products on CoPc@HC/Cu tandem electrode and $Cu_{1.5}$ electrode. The testing temperature is 25 ℃.

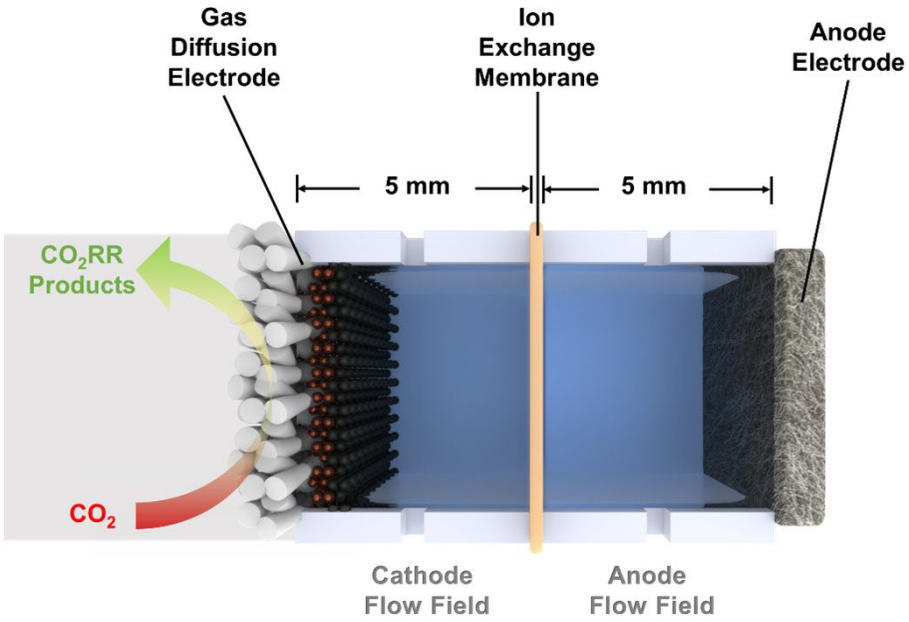

Supplementary Figure 46 | Schematics of slim flow cell. The cell was assembled by separating the cathode and anode compartment using a Nafion membrane and applying an equal compression torque to each of four bolts. When assembled, the distances between the Nafion membrane and cathode electrode and the Nafion membrane and anode electrode were both about 5 mm.

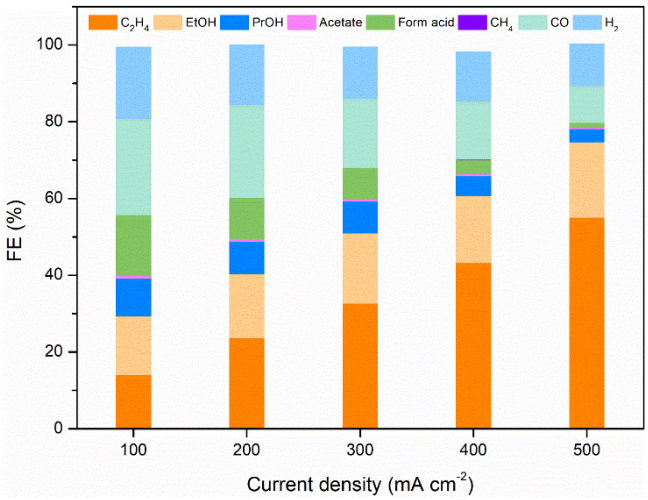

Supplementary Figure 47 | The acidic CO_2RR performance of CoPc@HC/Cu tandem electrode in a non-buffer of 0.05 M H_2SO_4 with 2.5 M KCl in slim flow cell. The testing temperature is 25 ℃.

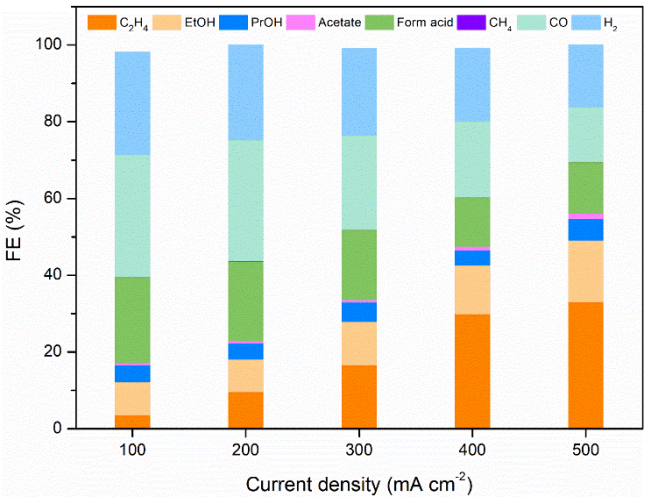

Supplementary Figure 48 | The acidic CO_2RR performance of Cu electrode in a non-buffer acidic electrolyte of 0.05 M H_2SO_4 with 2.5 M KCl in slim flow cell. The testing temperature is 25 ℃.

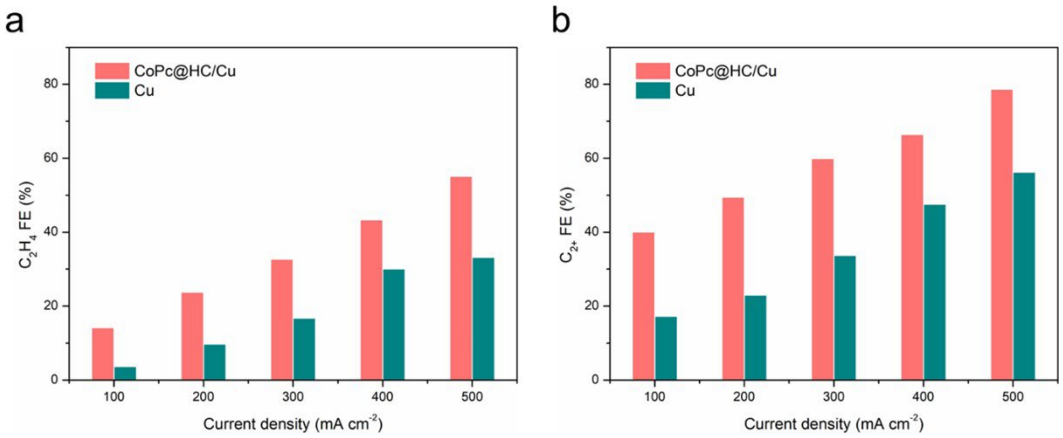

Supplementary Figure 49 | Performance comparison CoPc@HC/Cu electrode and Cu electrode in acidic CO_2RR in a non-buffer acidic electrolyte of 0.05 M H_2SO_4 with 2.5 M KCl in slim flow cell. **a**, C_2H_4 FE of CoPc@HC/Cu electrode and Cu electrode. **b**, C_{2+} FE of CoPc@HC/Cu tandem electrode and Cu electrode. The testing temperature is 25 ℃.

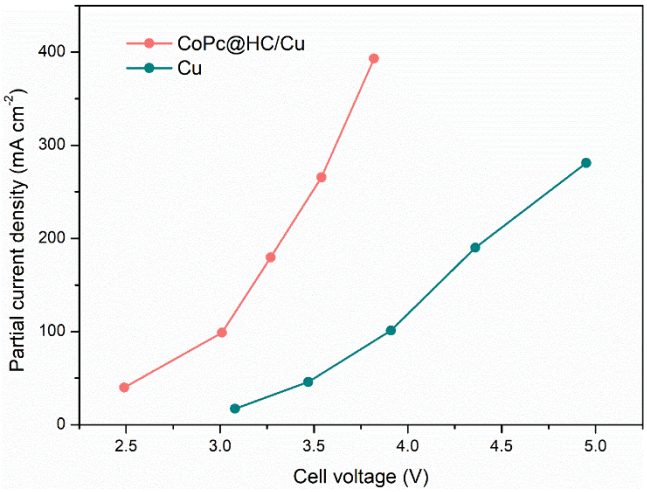

Supplementary Figure 50 | Partial current densities of C_{2+} products on CoPc@HC/Cu tandem electrode and Cu electrode in acidic CO_2RR in the slim flow cell. The testing temperature is 25 ℃.

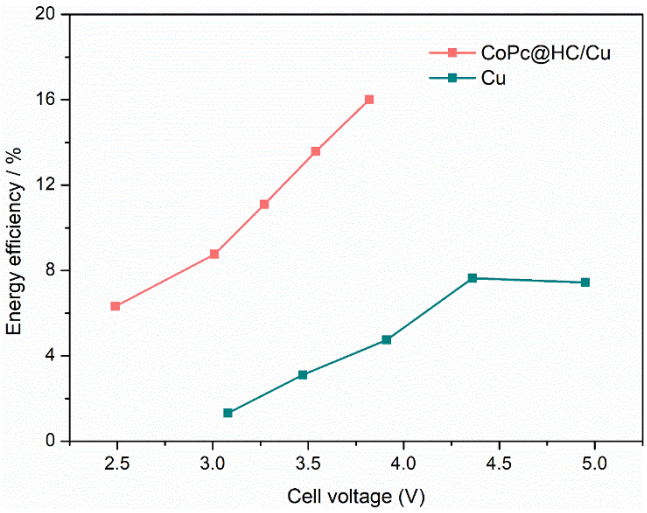

Supplementary Figure 51 | The energy efficiency of C_2H_4 production in acidic CO_2RR on CoPc@HC/Cu electrode and Cu electrode. The testing temperature is 25 ℃.

Supplementary Note 8 | Energy evolution for the CO_2RR system.

Energy analysis of the CO_2RR electrolyser was carried out by using an energy assessment model akin to that reported[14,15]. Here we provide a summary of the model and assumptions used to obtain the energy intensity of producing ethylene in an electrolyser using acid electrolytes. To calculate the energy intensity of producing ethylene, we used the main performance metrics of the electrolyser such as Faradaic efficiency, single-pass conversion efficiency, full-cell voltage, and current density as the input. We carried out the energy assessment under various operating conditions (e.g., at various CO_2 input flow rates) by using the readily achieved performance metrics as the input. We consider the presence of hydrogen produced via hydrogen evolution reaction (HER) at the cathodic product stream. We consider oxygen as the only product produced via oxygen evolution reaction (OER) at the anodic product stream. We implement a pressure swing adsorption (PSA) gas separation unit at the cathodic downstream to recover ethylene from the unreacted CO_2 and side product hydrogen. The recovered CO_2 from the cathode outlet is returned to the cathode inlet for utilization in the CO_2RR. Scaling up the electrolyte required for the lab-scale electrolysers, we considered an electrolyte requirement of 100 L per m^2 of electrolyser geometric area. The electrolyte is assumed to be circulated through a closed loop and used for 1 year without replacement. We provide further details of the energy calculations associated with the electrolyser electricity and cathode separation in Supplementary Note 9.

Supplementary Note 9 | Example calculation for the CO_2RR-to-ethylene conversion in a slim-flow cell.

This section provides an example calculation for the energy requirement associated with the electrolyser electricity and cathode separation in the CO_2-to-ethylene conversion process. The model uses the performance metrics of the slim-flow cell as the input. These metrics (Supplementary Table 4) include a Faradaic efficiency of 54%, a full-cell voltage of 3.76 V, a single pass conversion efficiency of 17%, and a current density of 500 mA cm^{-2}.

Electrolyser electricity. We begin by finding the production rate of ethylene on a molar basis per second, with a production capacity of 100 tons.

$$Production\ rate\ \left[\frac{mol}{s}\right] = \frac{Production\left[\frac{g}{day}\right]}{molecular\ weight_{ethylene}\left[\frac{g}{mol}\right] \times 86400\left[\frac{s}{day}\right]} \quad (1a)$$

$$Production\ rate\ \left[\frac{mol}{s}\right] = \frac{100 \times \frac{10^6 g}{day}}{\frac{28\ g}{mol} \times \frac{86400 s}{day}} = 41.335 \frac{mol}{s} \quad (1b)$$

We then determine the current required to produce ethylene at this rate for an experimentally achieved ethylene FE of 54%:

$$Total\ current\ required\ [A] = \frac{production\ rate\left[\frac{mol}{s}\right] \times electrons\ transferred \times Faraday's\ Constant}{FE_{ethylene}[decimal]} \quad (2a)$$

$$Total\ current\ needed\ [A] = \frac{41.335 \frac{mol}{s} \times 12 \times 96485 \frac{sA}{mol}}{0.54} = 88\,626\,832\ A \quad (2b)$$

We then multiply by the full-cell potential (3.76 V) to calculate the power consumed:

$$Power\ Consumed\ [W] = Total\ current\ needed\ [A] \times Cell\ voltage\ [V] = 88\,626\,832\ A \times 3.76\ V = 333237\ kW \quad (3)$$

To calculate the energy needed to run the plant for one day and meet the production capacity of 100 tons, we then multiply by 24 h:

$$Electricity\ Energy\ Requirement\ \left[\frac{GJ}{ton^{-1}}\right] = \frac{Power\ Consumed\ [W] \times 24[\mathrm{h}]}{daily\ production\ [ton]} = \frac{333237\ \mathrm{kW} \times 24\ \mathrm{h} \times 0.0036 \frac{\mathrm{GJ}}{\mathrm{kWh}}}{100\ ton} = \mathbf{288}\ \frac{\boldsymbol{GJ}}{\boldsymbol{ton}} \quad (4)$$

Cathode separation. To recover the ethylene from the cathodic downstream, we assumed a pressure swing adsorption (PSA) separation unit. The model accounts for the capital and operating costs of the PSA separation module based on a model for biogas upgrading. The cathodic gas stream is modelled to be composed of ethylene, unreacted CO_2, and hydrogen.

The model considers a cost of \$1 989 043 for a flow rate of 1000 m^3 h^{-1} by using a scaling factor of 0.7 and energy input of 0.25 kWh m^{-3}. In light of these, we calculate the energy consumption as follows.

$$PSA\ Operating\ Energy\ \left[\frac{\text{kWh}}{ton\ ethylene}\right] = 0.25\ \frac{kWh}{m^3} \times flow\ rate\left[\frac{m^3}{h}\right] \times 24\frac{h}{day} \quad (5a)$$

Before using this equation, we calculate the flow rate of the cathodic stream: we determined the flow rate of ethylene under the standard conditions as follows.

$$Output\ ethylene\ flow\ rate\ \left[\frac{m^3}{h}\right] = \frac{100 \times 10^6\ g \times 8.314\ Jmol^{-1}K^{-1} \times 298K}{28\frac{g}{mol} \times 101\,300\ Pa \times 24\frac{h}{day}} = 3639\ \frac{m^3}{h} \quad (6)$$

We calculate the flow rates of unreacted CO_2, product ethylene, and by-product hydrogen at the cathode outlet. The flow rate of unreacted CO_2 at the cathode outlet is calculated by using the single pass conversion efficiency at a constant pressure. It is worth noting that this single pass conversion efficiency merely relates to the amount of CO_2 reduced to the CO_2 that passes through the cathode stream, unreacted. Considering a single-pass conversion of 17%, we have:

$$Output\ CO_2\ flow\ rate\ \left[\frac{m^3}{h}\right] =$$

$$ethylene\ flow\ rate\ \left[\frac{m^3}{h}\right] \times molar\ ratio\ \left[\frac{CO_2}{ethylene}\right] \times \left(\frac{100 - single\ pass\ conversion[\%]}{single\ pass\ conversion[\%]}\right) \quad (7a)$$

$$Output\ CO_2\ flow\ rate\ \left[\frac{m^3}{h}\right] = 3639\frac{m^3}{h} \times 2 \times \frac{100-17}{17} = 35533\ \frac{m^3}{h} \quad (7b)$$

Since H_2 is the only by product at the cathode stream, we can determine the current toward H_2 as:

$$Current\ toward\ H_2[A] = Total\ current\ needed[A] \times \frac{100 - FE_{ethylene}[\%]}{100} \quad (8a)$$

$$Current\ toward\ H_2[A] = 88\,626\,832\ A \times \frac{100-54}{100} = 40\,7683\,42\ A \quad (8b)$$

The H_2 production rate can be defined as follows.

$$H_2\ production\ \left[\frac{mol}{h}\right] = \frac{Current\ toward\ H_2[A] \times 3600\frac{s}{h}}{2\frac{electrons}{H_2\ product} \times Faraday's\ Constant} \quad (9a)$$

$$H_2\ production\ \left[\frac{mol}{h}\right] = \frac{40\,768\,342\ A \times 3600\frac{s}{hour}}{2\frac{electrons}{H_2\ product} \times 96485\frac{sA}{mol}} = 760\,563\ \frac{mol}{h} \quad (9b)$$

Assuming an ideal gas under standard conditions, we calculate the flow rate of H_2:

$$flow\ rate_{H2}\left[\frac{m^3}{h}\right] = \frac{H_2\ production\left[\frac{mol}{h}\right] \times 8.314 \frac{J}{mol \times K} \times 298K}{101.3 \times 10^3 Pa} \quad (10a)$$

$$flow\ rate_{H2}\left[\frac{m^3}{h}\right] = \frac{760\,563 \frac{mol}{h} \times 8.314 \frac{J}{mol \times K} \times 298K}{101.3 \times 10^3 Pa} = 18\,601\ \frac{m^3}{h} \quad (10b)$$

We then calculate the total flow rate at the cathodic downstream by summing the flow rate of ethylene, unreacted CO_2, and H_2.

$$flow\ rate\left[\frac{m^3}{h}\right] = (3639 + 35533 + 18601)\frac{m^3}{h} = 57\,773\frac{m^3}{h} \quad (11)$$

With the final output flow rate, we can then calculate the energy required per ton of ethylene produced using Supplementary Equation 5a:

$$\text{PSA Energy}\left[\frac{\text{GJ}}{\text{ton ethylene}}\right] = 0.25\ \frac{\text{kWh}}{\text{m}^3} \times 57\,773 \frac{\text{m}^3}{\text{h}} \times 24 \frac{\text{h}}{\text{day}} \times \frac{0.0036\ \text{GJ kWh}^{-1}}{100\ \text{ton ethylene}}$$
$$= \mathbf{12}\ \frac{\mathbf{GJ}}{\mathbf{ton\ ethylene}} \quad (5b)$$

Energy calculations toward C_{2+} products. Energy cost of producing C_{2+} products is estimated by using the similar calculations for the electrolyser electricity and cathode separation energy costs. As ethylene is the dominant C_2 product, the electrolyser electricity cost is made using the molecular mass and electron transfer numbers for ethylene, and this leads to a more conservative energy requirement. An extra energy input of ~25 GJ ton^{-1} associated with the liquid product distillation is estimated by using an empirical formula reported[16]. This estimation reflects the highly diluted liquid product concentration in the acidic electrolytes, which is assumed to be 0.5% wt%.

Supplementary Table 4 | Product FEs on CoPc@HC/Cu tandem electrode and Cu electrode in acidic CO_2RR under the applied current density of 500 mA cm^{-2} with CO_2 flow rate of 4 sccm in slim flow cell at 25 °C.

Electrodes	Full cell voltage (V)	H_2 FE(%)	CO FE(%)	C_2H_4 FE(%)	CH_4 FE(%)	EtOH FE(%)	Acetate FE(%)	Formate FE(%)	Propanol FE(%)
CoPc@HC/Cu	3.76	13.2	9.6	53.6	0.01	16.2	1.9	3.1	2.5
Cu	4.70	42.1	9.1	30.2	0.1	11.8	1.7	2.9	2.1

Supplementary Table 5 | Energy assessment of producing ethylene and C_{2+} in acidic media at 25 °C.

Parameters	Current best C_2H_4 (Science 2021)[11]	Cu electrode C_2H_4 (This work)	CoPc@HC/ Cu C_2H_4 (This work)	Current best C_{2+} (Science 2021)[11]	Cu electrode C_{2+} (This work)	CoPc@HC/Cu C_{2+} (This work)
Cell voltage (V)	4.2	4.70	3.76	4.2	4.70	3.76
Faradaic efficiency (%)	29	30	54	44	46	74
Current density (mA cm^{-2})	1200	500	500	1200	500	500
Electrolyser specific energy distribution (GJ/(tonne ethylene or C_{2+})$^{-1}$)						
Electrolyser electricity	599	648	288	395	423	210
Cathode separation	16	26	12	9	15	7
Anode separation (Carbonate)	0.0	0.0	0.0	0.0	0.0	0.0
Carbonate regeneration	0.0	0.0	0.0	0.0	0.0	0.0
Liquid product distillation	-	-	-	25	25	25
Overall energy (GJ/ton)	**615**	**674**	**300**	**429**	**463**	**242**

Supplementary Table 6 | Energy assessment of producing ethylene of CoPc@HC/Cu tandem electrode system in comparison to the benchmark of alkaline/neutral/acidic systems at 25 °C.

Parameters	Alkaline media CO_2RR[12] (*Science* 2018, 360, 783-787.)	Neutral media CO_2RR[17] (*Nature* 2020, 577, 509–513.)	Acidic media CO_2RR[11] (*Science* 2021, 372, 1074-1078.)	Acidic media CO_2RR CoPc@HC/Cu (This work)
Cell voltage (V)	2.5	3.65	4.2	3.76
Faradaic efficiency (%)	70	64	29	54
Current density (mA cm^{-2})	150	120	1200	500
	Electrolyser specific energy distribution (GJ/(tonne ethylene)$^{-1}$)			
Electrolyser electricity	142	235	599	288
Cathode separation	144	133	16	12
Anode separation	0.0	68	0.0	0.0
Carbonate regeneration	278	0.0	0.0	0.0
Overall energy (GJ/ton)	**564**	**436**	**615**	**300**

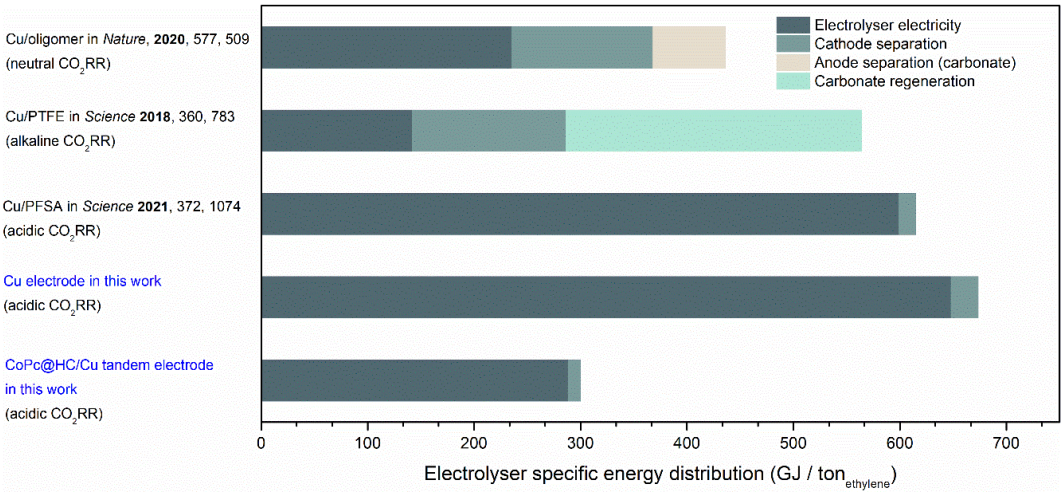

Supplementary Figure 52 | The energy intensity for the production of C_2H_4 on CoPc@HC/Cu tandem electrode and Cu electrode as well as the benchmark of prior alkaline/neutral/acidic system based on the Supplementary Tables 4-6.

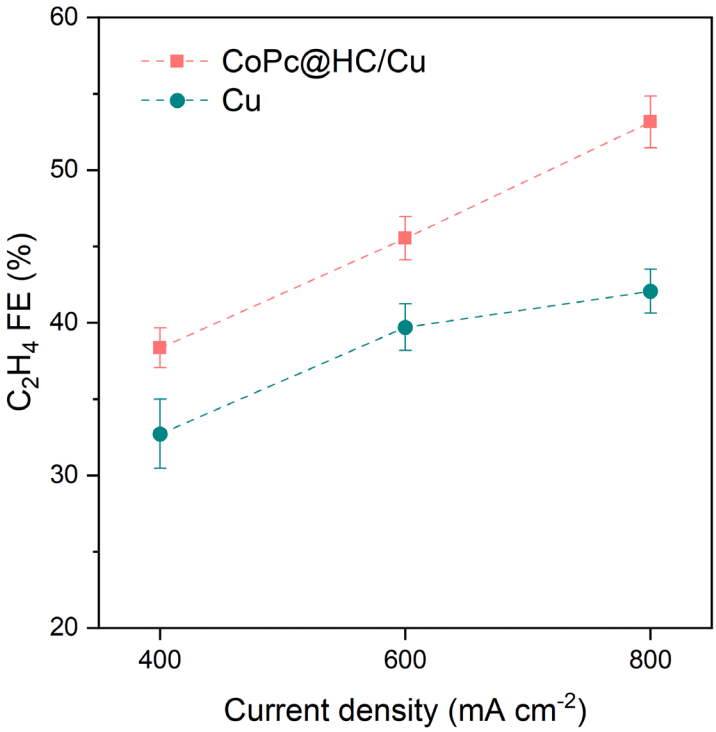

Supplementary Figure 53 | C_2H_4 FE of CoPc@HC/Cu tandem electrode and Cu electrode in CO reduction reaction (CORR) performance in the acidic buffer electrolyte of 0.5 M H_3PO_4 and 0.5 M KH_2PO_4 with 2.5 M KCl. Error bars represent the standard deviation of three independent measurements (n=3). Data are presented as mean values. The testing temperature is 25 ℃.

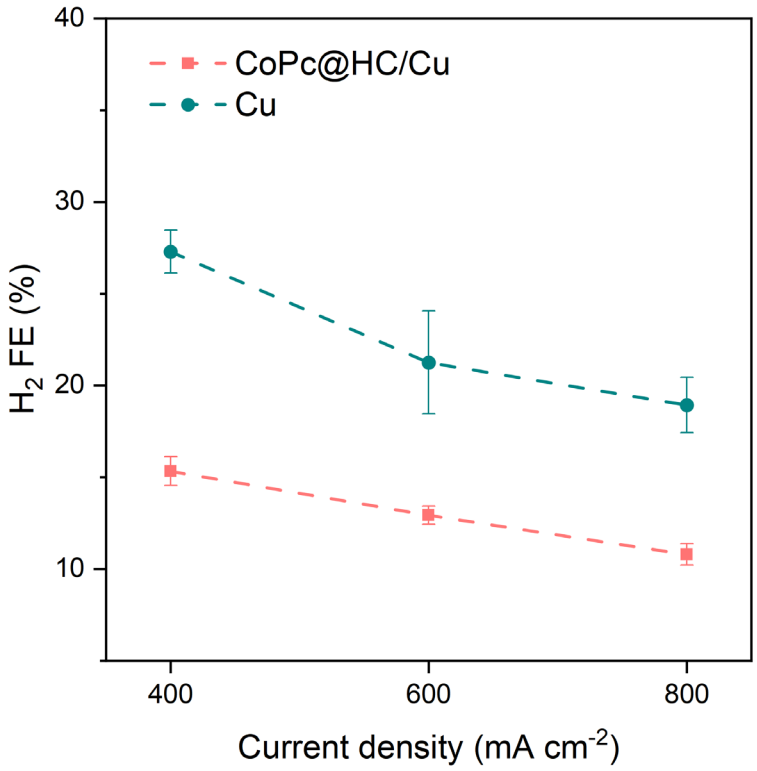

Supplementary Figure 54 | H_2 FE of CoPc@HC/Cu tandem electrode and Cu electrode in CO reduction reaction (CORR) performance in the acidic buffer electrolyte of 0.5 M H_3PO_4 and 0.5 M KH_2PO_4 with 2.5 M KCl. Error bars represent the standard deviation of three independent measurements (n=3). Data are presented as mean values. The testing temperature is 25 ℃.

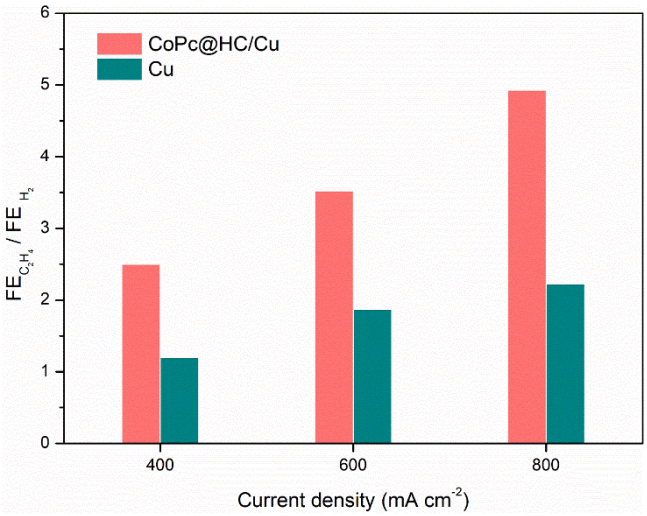

Supplementary Figure 55 | Comparison of the ratio of C_2H_4 FE and H_2 FE on CoPc@HC/Cu tandem electrode and Cu electrode in CO reduction reaction performance in the acidic buffer electrolyte of 0.5 M H_3PO_4 and 0.5 M KH_2PO_4 with 2.5 M KCl. CoPc@HC/Cu tandem electrode exhibits obviously higher C_2H_4 FE and lower H_2 FE in CORR compared to CO_2RR from 400 to 800 mA cm^{-2}, suggesting, besides reducing CO_2 to CO and suppressing the evolution of H_2 in acidic media, the CoPc@HC catalyst layer was able to accelerate C-C coupling to C_2H_4. The testing temperature is 25 ℃.

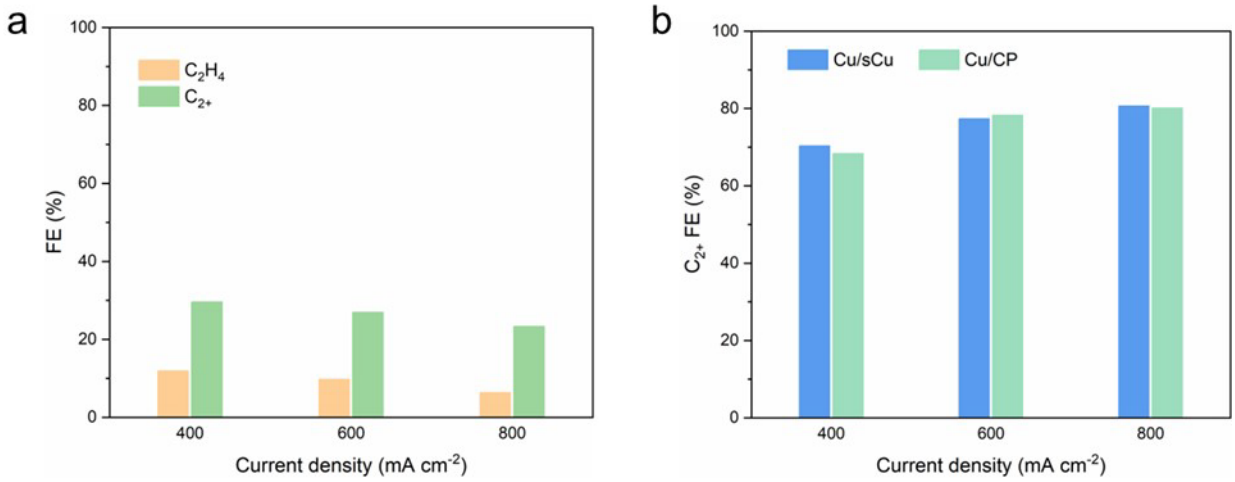

Supplementary Figure 56 | a, the FEs of C_2H_4 and C_{2+} in CORR on the sputtered Cu in an acidic buffer electrolyte of 0.5 M H_3PO_4 and 0.5 M KH_2PO_4 with 2.5 M KCl in flow cell. **b**, Comparison of C_{2+} FE on Cu electrode with sputtered as a conductive gas-diffusion layer (Cu/sCu) and Cu electrode with carbon paper as a conductive gas-diffusion layer (Cu/CP). The testing temperature is 25 ℃.

The sputtered Cu showed about 12% C_2H_4 FE and 33% C_{2+} FE at 400 mA cm^{-2} (Supplementary Fig. 56a). With the increase of current density, the FEs of C_2H_4 and C_{2+} gradually decreased. The sputtered Cu exhibited about 6% C_2H_4 FE and 23% C_{2+} FE at 800 mA cm^{-2}. In our work, the sputtered Cu on the PTFE was used as a conductive gas-diffusion layer to prepare the Cu electrode by spraying ionomer-modified Cu nanoparticles onto it. To investigate the contribution of the sputtered Cu in the Cu electrode, we also prepared the Cu electrode on carbon paper by spraying ionomer-modified Cu nanoparticles onto carbon paper. The performance of Cu electrode on carbon paper (Cu/CP) is similar to that of Cu electrode on sputtered Cu (Cu/sCu) (Supplementary Fig. 56b), suggesting the sputtered Cu has little effect on the performance when the ionomer-modified Cu nanoparticles are existed.

Supplementary Note 10 | The interfacial structure between CoPc@HC and Cu nanoparticles.

We carried out the high-resolution transmission electrode microscopy (HRTEM) measurements to examine the contacts between CoPc@HC and Cu nanoparticle (Cu NP) in the CoPc@HC/Cu electrode. The HRTEM image shows that there is contact between CoPc@HC particle and Cu NP, with some gaps existing between them (Supplementary Fig. 57a and b). The obvious disordered lattice fringe is associated with the carbon support of CoPc@HC particle. The lattice fringe of 0.21 nm is corresponding to the (111) crystal plane of Cu NP. The EDS mapping analysis shows that the perfluorosulfonic acid (PFSA) ionomer is also observed on the Cu surface (Supplementary Fig. 58). In the HRTEM mode, the intensity of transmitted electrons is closely related to the atomic number density of the sample. As the transmitted electrons pass through the sample, they interact with the atoms in the sample, including scattering, absorption, and diffraction processes, which can cause the intensity of the transmitted electrons to weaken. As a simplification, the regions with higher the atomic number density of the sample usually appear darker, and the corresponding intensity is weaker. In addition, the crystalline sample should show lattice fringes due to diffraction contrast which the amorphous counterpart lack of. As shown in Supplementary Fig. 57b, the crystalline and the amorphous section were distinguished according to the invers FFT pattern, and then, emphasized the edge of each section by white dashed lines. The thickness contrast, the lattice fringe and the intensity profiles suggest that there are some gap regions between the CoPc@HC particle and the Cu NP (Supplementary Fig. 57c-f). The widths of the gap regions were estimated to be typically less than 1 nm, indicating the existence of sub-nanometer-thick spaces between CoPc@HC and Cu particles, which is consistent with our theoretical model.

In this work, we noted that the sub-nanometer-thick spaces between CoPc@HC and Cu NP could promote the C_2H_4 production by control experiments and DFT calculation. To evaluate this point, we designed a controlled electrode (denoted as CoPc@HC/C/Cu) to eliminate the sub-nanometer-thick spaces by adding a carbon layer between CoPc@HC and Cu NP (Supplementary Fig. 62). The CoPc@HC/C/Cu exhibits a lower C_2H_4 FE than CoPc@HC/Cu in the current density range from 400 to 800 mA cm^{-2}, suggesting the sub-nanometer-thick

spaces between CoPc@HC and Cu NP contributed to an enhancement on C_2H_4 FE in acidic CO_2RR. We also evaluated the performance of CoPc@HC/C/Cu in acidic CORR where the CO availability is not a limiting factor in C_2H_4 formation. The C_2H_4 FE on CoPc@HC/C/Cu is similar with that of Cu electrode, while is lower than that of CoPc@HC/Cu, suggesting the sub-nanometer-thick spaces between CoPc and Cu could facilitate C_2H_4 production.

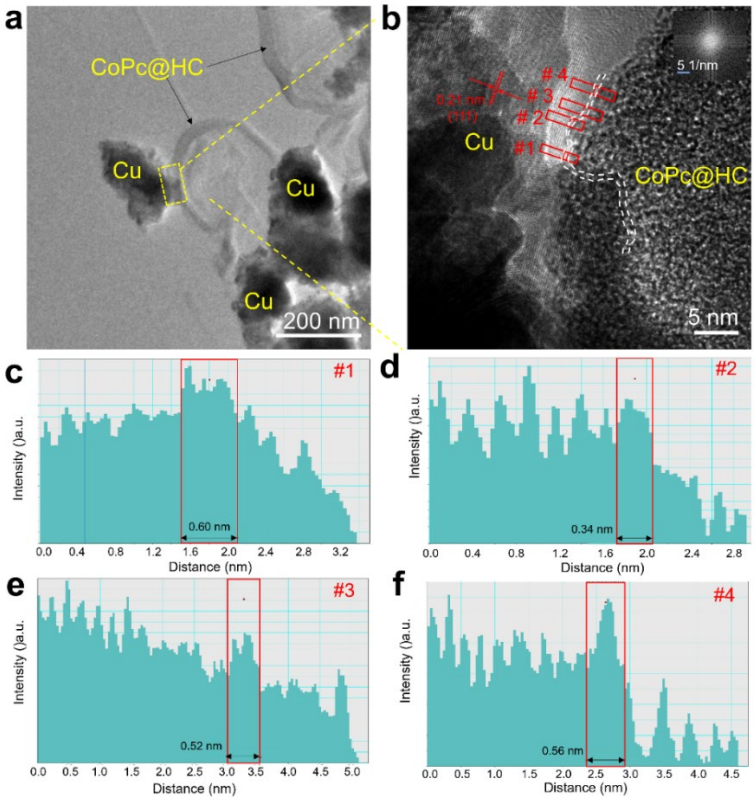

Supplementary Figure 57 | Structural characterization of CoPc@HC/Cu by HRTEM measurement. a-b HRTEM image (a) and enlarged HRTEM image (b) of CoPc@HC/Cu. The enlarged HRTEM image was taken from corresponding yellow rectangular areas. **c-f**, The intensity profiles taken along the red rectangular frames in **b**, showing the gap width between CoPc@HC and Cu particles.

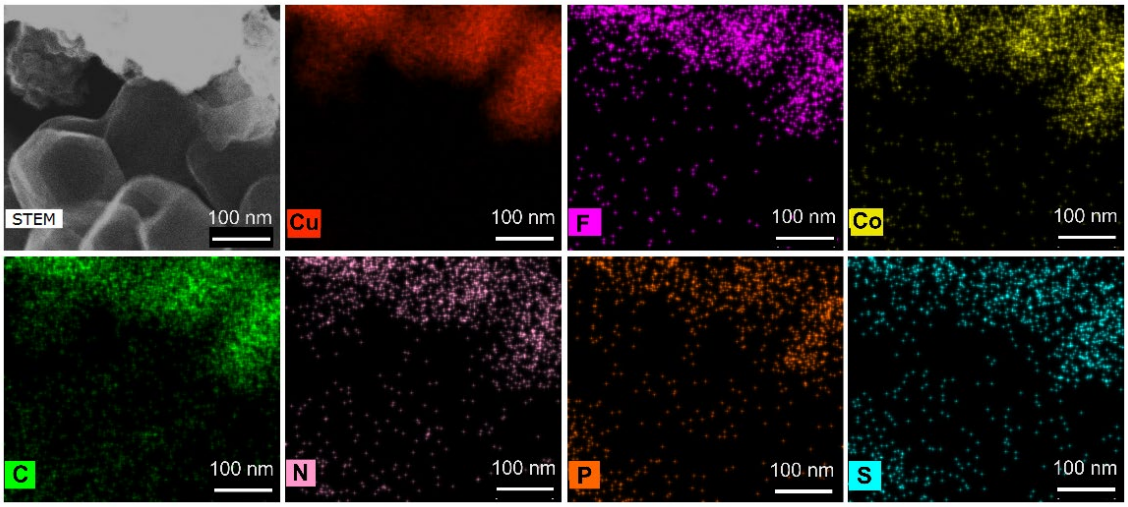

Supplementary Figure 58 | HAADF-STEM image and the corresponding elemental energy-dispersive X-ray spectroscopy (EDS) mapping images of CoPc@HC/Cu. Perfluorosulfonic acid (PFSA) ionomer exhibits differentiated hydrophilic and hydrophobic characteristics endowed by $-SO_3^-$ and $-CF_2$ functionalities, respectively. The elemental EDS mapping of F image reveal that the presence of continuous ionomer coating on Cu nanoparticles.

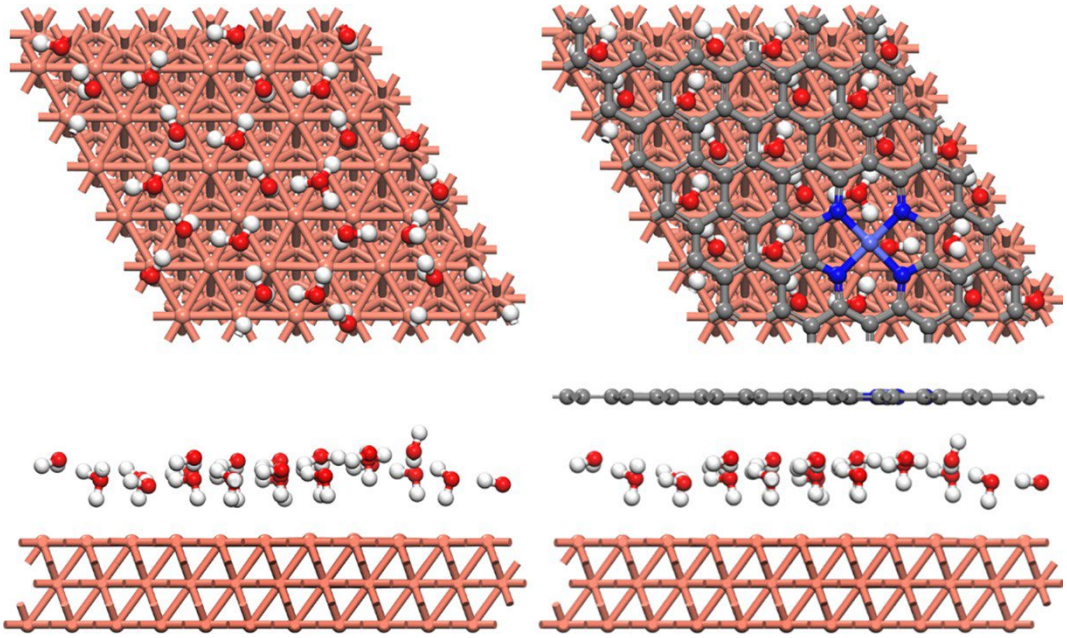

Supplementary Figure 59 | The model of (6×6) Cu(111) covered a charged water-layer consisting of twenty-four molecules with/without two-dimensional CoN_4-Graphene structure.

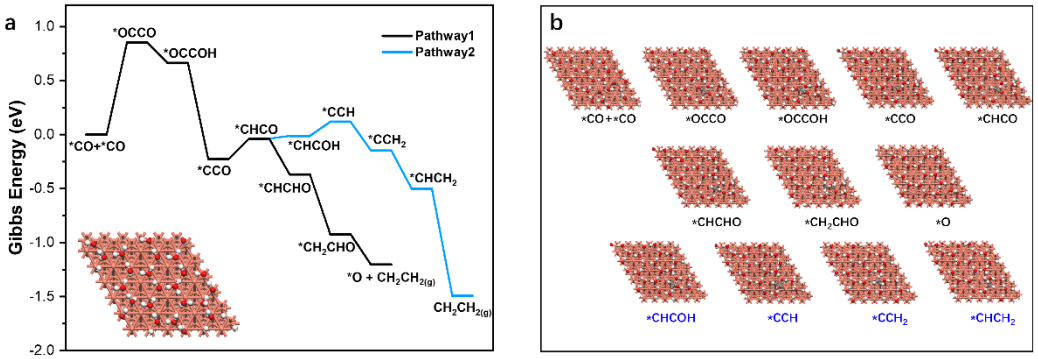

Supplementary Figure 60 | Free energy diagram of the production of C_2H_4 on Cu(111). a, Two possible reaction pathways on Cu(111). **b**, The corresponding atomic configuration for each reaction intermediate.

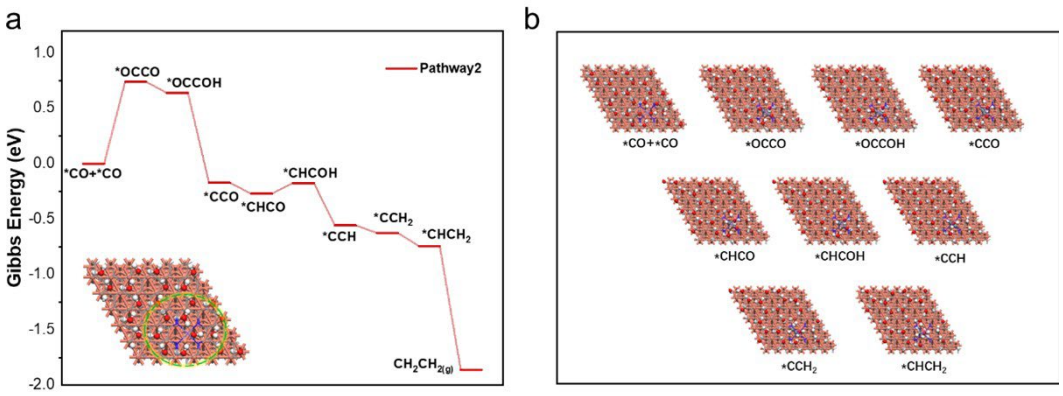

Supplementary Figure 61 | Free energy diagram of the production of C_2H_4 on CoN_4-C/Cu(111). a, The possible reaction pathway on the CoN_4-C/Cu(111). **b**, The corresponding atomic configuration for each reaction intermediate. Under the influence of CoN_4-C structure, the pathway1 same with Supplementary Figure 60 does not exist because the key intermediate *CHCHO is hard to stabilize adsorption on Cu(111).

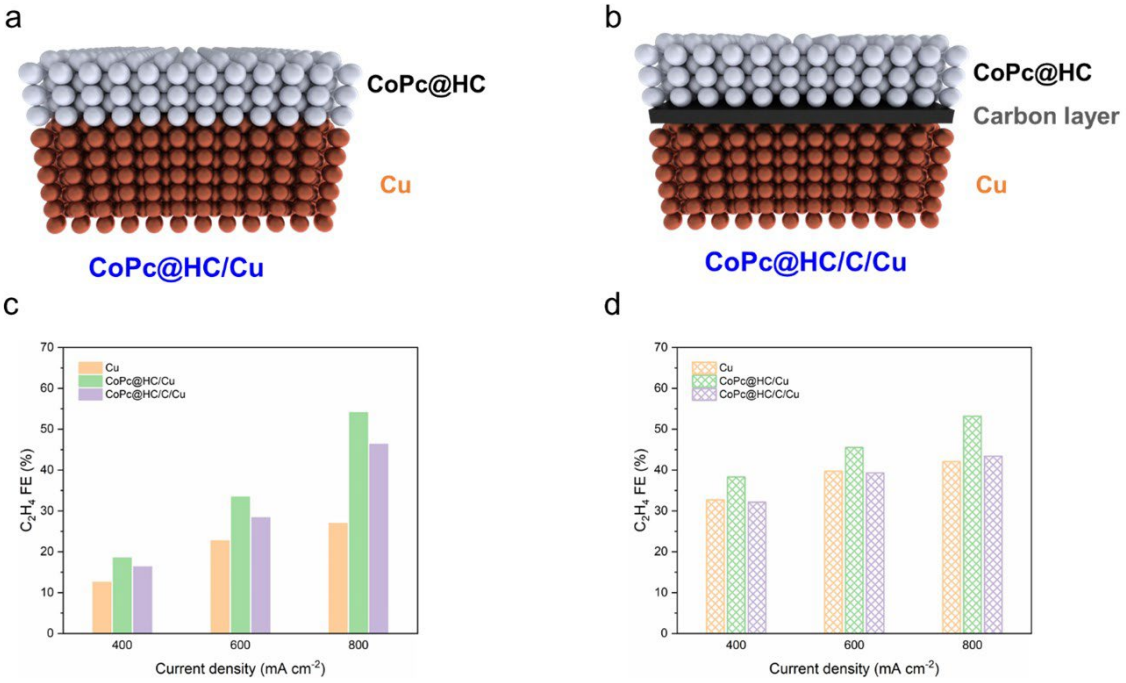

Supplementary Figure 62 | a-b, Schematics of CoPc@HC/Cu electrode and CoPc@HC/C/Cu electrode. **c-d**, C_2H_4 FE on Cu electrode, CoPc@HC/Cu electrode and CoPc@HC/C/Cu electrode in the acidic buffer electrolyte of 0.5 M H_3PO_4 and 0.5 M KH_2PO_4 with 2.5 M KCl in flow cell in CO_2RR performance (**c**) and CORR performance (**d**). The testing temperature is 25 ℃.

We designed a controlled electrode (denoted as CoPc@HC/C/Cu) to eliminate the sub-nanometer-thick spaces by adding a carbon layer between CoPc@HC and Cu NP. The CoPc@HC/C/Cu exhibits a lower C_2H_4 FE than CoPc@HC/Cu, suggesting the sub-nanometer-thick spaces between CoPc@HC and Cu NP contributed to an enhancement on C_2H_4 FE in acidic CO_2RR. We also evaluated the performance of CoPc@HC/C/Cu in acidic CORR where the CO availability is not a limiting factor in C_2H_4 formation. The C_2H_4 FE on CoPc@HC/C/Cu is similar with that of Cu electrode, while is lower than that of CoPc@HC/Cu, indicating the sub-nanometer-thick spaces between CoPc and Cu could facilitate C_2H_4 production.

Supplementary Note 11 | The structure, composition, and performance of CoPc@HC/(Cu+CoPc@HC) tandem electrode.

We further increased the sub-nanometer-thick spaces by mixing Cu nanoparticles and CoPc@HC particles to form (Cu+CoPc@HC) catalyst layer (Supplementary Figs. 63 and 64**)**. The Cu NPs are in contact with CoPc@HC particles. The enlarged HRTEM images show that the sub-nanometer-thick spaces between Cu and CoPc@HC particles. We further employed (Cu+CoPc@HC) catalyst layer to replace Cu NP catalyst layer to form CoPc@HC/(Cu+CoPc@HC) electrode. With improved sub-nanometer-thick spaces, the CoPc@HC/(Cu+CoPc@HC) exhibited an obvious enhancement on C_2H_4 FE compared with CoPc@HC/Cu electrode in acidic CO_2RR (Supplementary Fig. 65). Notably, a maximum C_2H_4 FE of 61% was achieved on the CoPc@HC/(Cu+CoPc@HC) at 800 mA cm^{-2}. The CoPc@HC/(Cu+CoPc@HC) electrode also exhibited an SPCE of 90% ± 3%; this high SPCE was achieved simultaneously with a C_2H_4 FE of 55% ± 3% C_2H_4 FE and a total C_{2+} FE of 76% ± 2% at 800 mA cm^{-2} with a CO_2 flow rate of 2 ml min^{-1}. These results suggested that the sub-nanometer-thick spaces between CoPc and Cu could favor ethylene production, which is consistent with our DFT results that CoPc working in conjunction with Cu promote C_2H_4 selectivity.

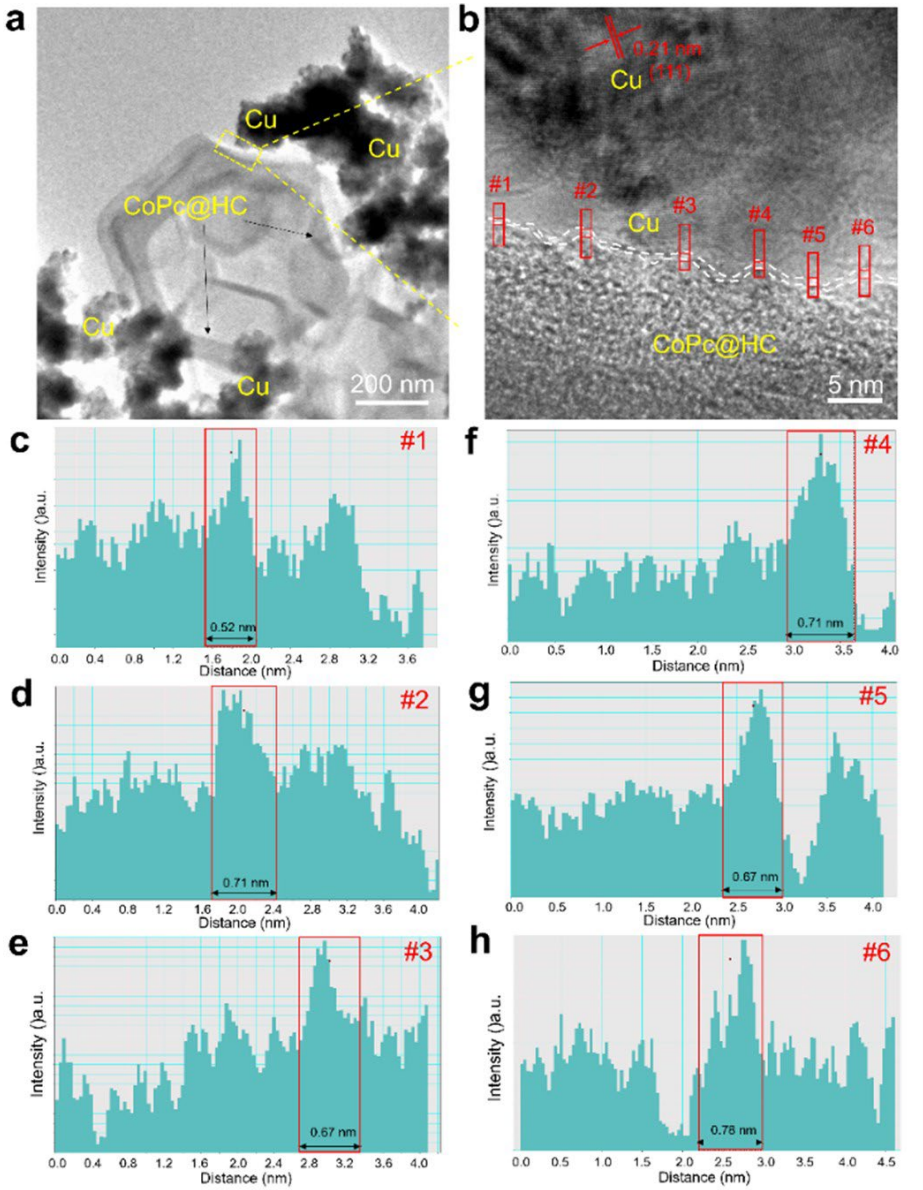

Supplementary Figure 63 | Structural characterization of (Cu+CoPc@HC) catalyst layer by HRTEM measurement. a-b, HRTEM image (**a**) and enlarged HRTEM image (**b**) of (Cu+CoPc@HC). The enlarged HRTEM image was taken from corresponding yellow rectangular areas. **c-h**, The intensity profiles taken along the red rectangular frames in **b**, showing the gap width between CoPc@HC and Cu particles.

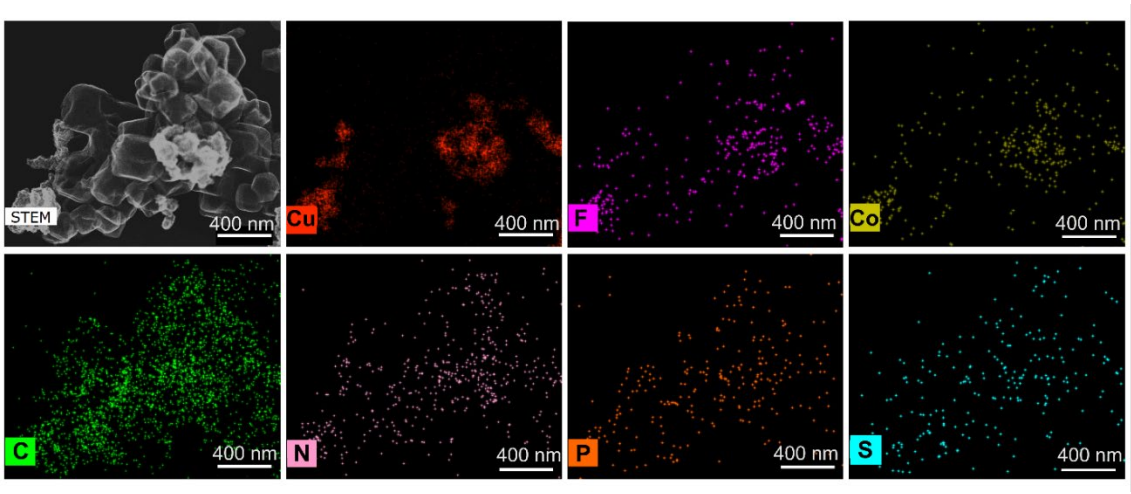

Supplementary Figure 64 | HAADF-STEM image and the corresponding elemental energy-dispersive X-ray spectroscopy (EDS) mapping images of (Cu+CoPc@HC) catalyst layer. Perfluorosulfonic acid (PFSA) ionomer exhibits differentiated hydrophilic and hydrophobic characteristics endowed by $-SO_3^-$ and $-CF_2$ functionalities, respectively. The elemental EDS mapping of F image reveal that the presence of continuous ionomer coating on Cu nanoparticles.

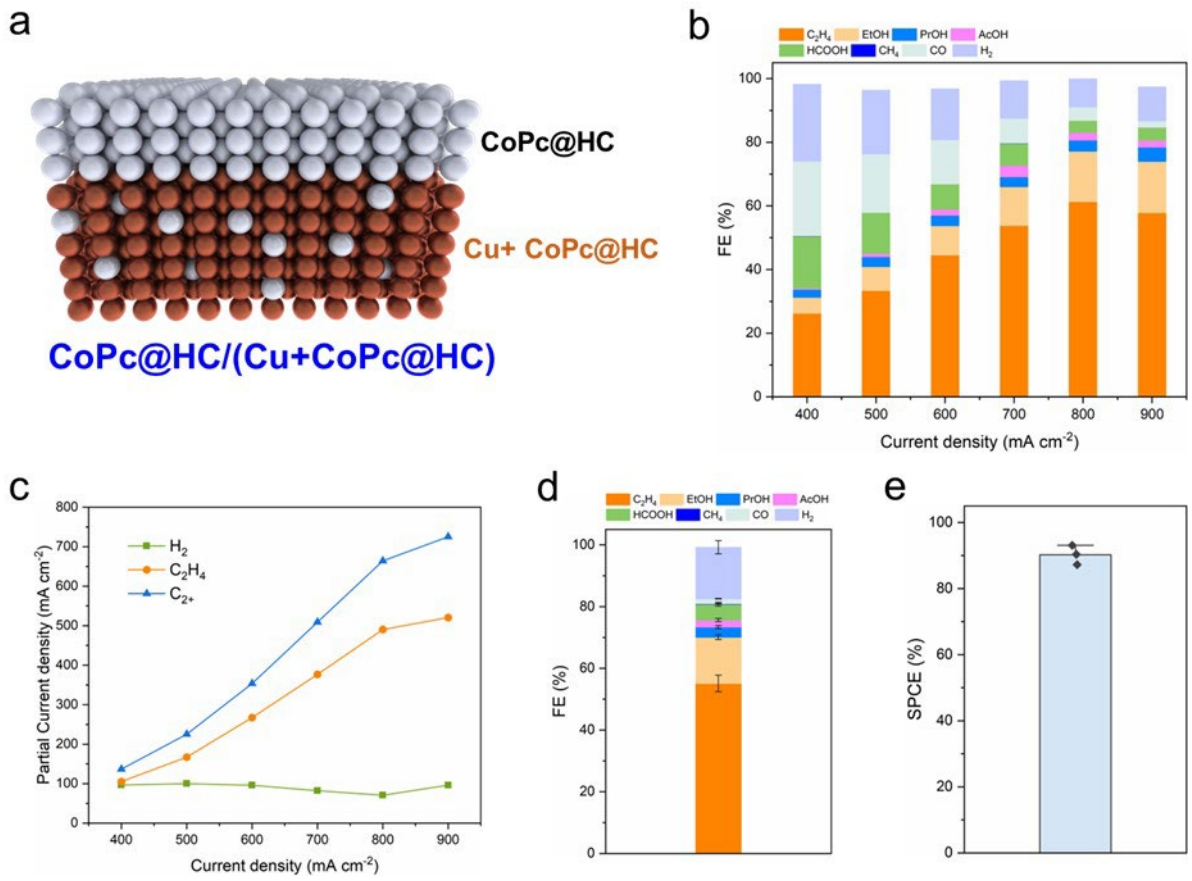

Supplementary Figure 65 | Acidic CO_2RR performance of CoPc@HC/(Cu+CoPc@HC) tandem electrode in an acidic buffer electrolyte of 0.5 M H_3PO_4 and 0.5 M KH_2PO_4 with 2.5 M KCl in flow cell at 25 °C. a, Schematic of CoPc@HC/(Cu+CoPc@HC) tandem electrode. **b**, FEs of CO_2RR products on CoPc@HC/(Cu+CoPc@HC) tandem electrode. **c**, Partial current densities of H_2, C_2H_4 and C_{2+} on CoPc@HC/(Cu+CoPc@HC) tandem electrode. **d-e**, FEs of CO_2RR products (**d**) and SPCE (**e**) on CoPc@HC/(Cu+CoPc@HC) tandem electrode at 800 mA cm^{-2} with a CO_2 inlet flow rate of 2 ml min^{-1}. Values are means, and error bars represent the standard deviation from three independent measurements (n=3).

Supplementary Note 12 | Carbon balance analysis.

In the CO_2 reduction reaction (CO_2RR) system, CO_2 is either converted into CO_2RR products; or is released from the system either in the form of (bi)carbonate or as unreacted CO_2[11,15,18]. In the alkaline electrolyte CO_2RR system (Supplementary Fig. 66a), CO_2 is captured at the cathode/catholyte interface and is converted to CO_3^{2-} and HCO_3^-, and these keep accumulating in the alkaline aqueous environment. In the neutral electrolyte CO_2RR system, CO_2 is also captured at the cathode/catholyte interface and forms CO_3^{2-} and HCO_3^-. These species then pass through the anion exchange membrane and evolve into CO_2 gas, which is subsequently released along with anodic oxygen (Supplementary Fig. 66b). In contrast, in the acidic electrolyte CO_2RR system, the CO_3^{2-} and HCO_3^- formed at cathode/catholyte interface are converted back into CO_2 molecules locally and actively participate in the cathodic electrochemical reaction (Supplementary Fig. 66c).

To analyze the carbon balance of this system, we first monitored the catholyte pH and found that it became stable within 30 min, i.e. the system reached a steady state (Supplementary Fig. 67). We then performed three independent measurements to assess the carbon balance by investigating CO_2 in the anode outlet, CO_2 in the cathode outlet, CO_2 to products (i.e. CO_2 utilization) and CO_2 in electrolyte (Supplementary Fig. 68). We measure that in the acidic CO_2RR system, less than 2% of the initial input CO_2 is released from the anode outlet. In contrast, approximately 70% of the consumed CO_2 is released from the anode outlet in the alkaline and neutral electrolyte CO_2RR systems[11,18]. The single pass carbon efficiency (SPCE) of CO_2 in our acidic CO_2RR system reached 90%±3% when operated at 800 mA cm^{-2} with a CO_2 flow rate of 2 ml min^{-1} (Supplementary Fig. 65d).

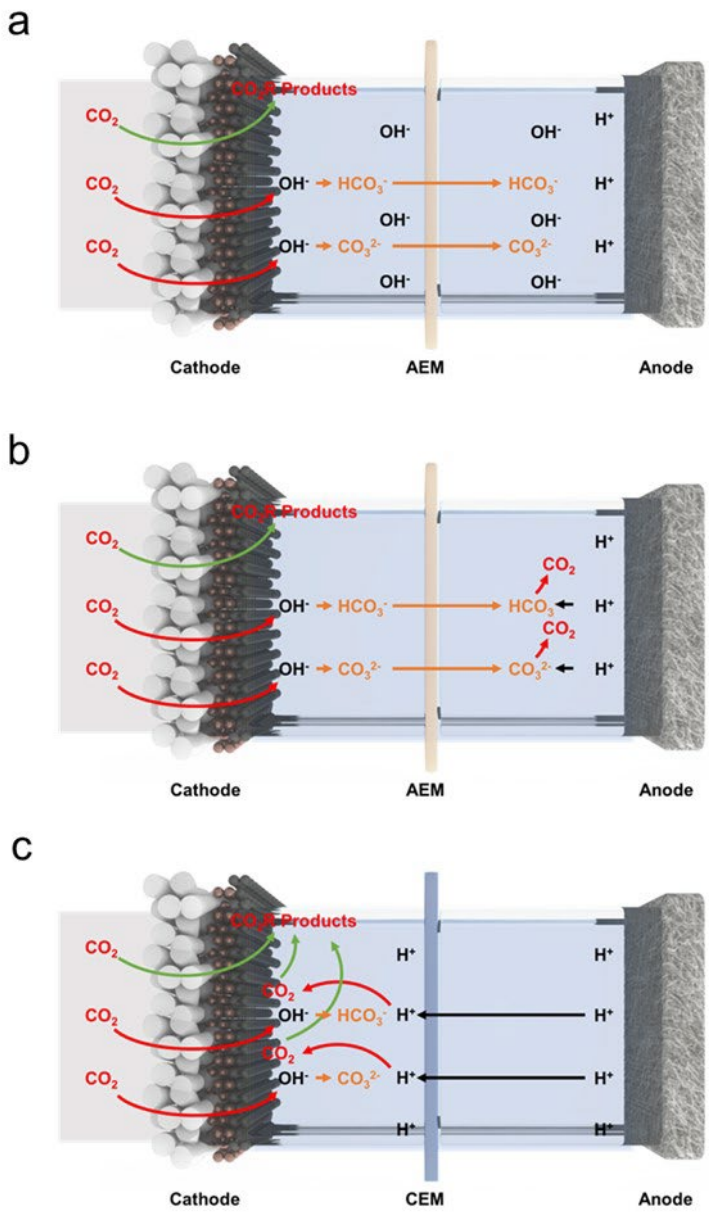

Supplementary Figure 66 | Schematic illustration of carbon balance paths of CO_2RR in alkaline electrolyte (**a**), in neutral electrolyte (**b**) and in acidic electrolyte (**c**).

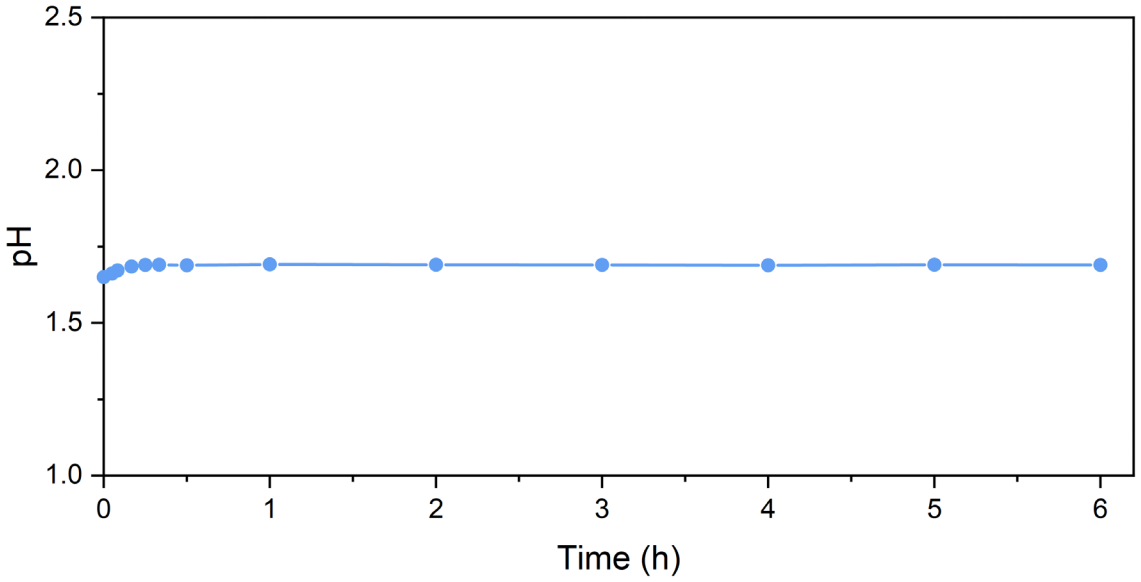

Supplementary Figure 67 | pH values of catholyte under operating acidic CO_2RR on a CoPc@HC/(Cu+CoPc@HC) tandem electrode at 800 mA/cm^2 in acidic buffer electrolyte of 0.5 M H_3PO_4 and 0.5 M KH_2PO_4 with 2.5 M KCl in a flow cell electrolyser with a CO_2 flow rate of 2 ml min^{-1}. The testing temperature is 25 ℃.

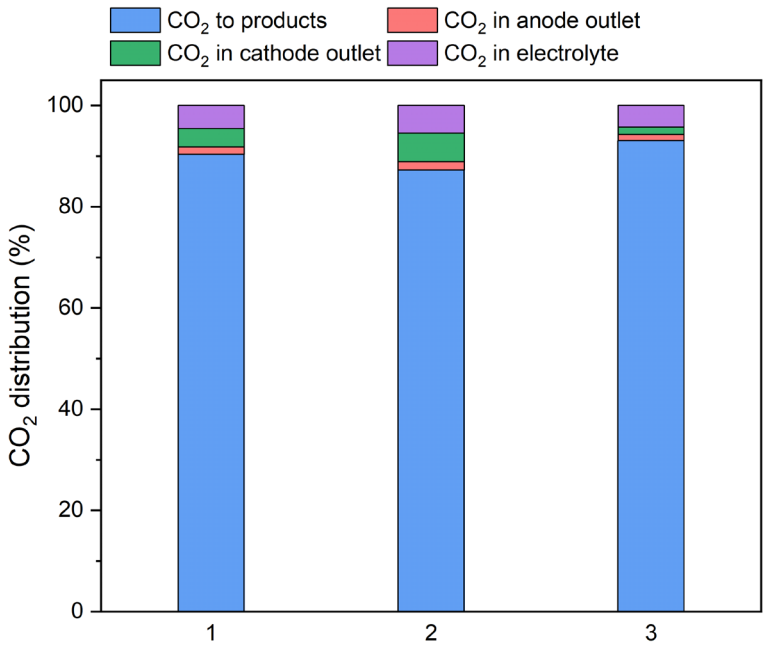

Supplementary Figure 68 | Three independent measurements for carbon balance analysis under operating acidic CO_2RR on a CoPc@HC/(Cu+CoPc@HC) tandem electrode at 800 mA/cm^2 in acidic buffer electrolyte of 0.5 M H_3PO_4 and 0.5 M KH_2PO_4 with 2.5 M KCl in a flow cell electrolyser with 2 ml min^{-1} CO_2 as feeding gas. The testing temperature is 25 °C. CO_2 to products means the consumed CO_2 for reduction reaction to all liquid and gas products determined by NMR and GC. CO_2 in anode outlet is the residual CO_2 flow in anode outlet due to CO_2 crossover determined by GC. CO_2 in cathode outlet is the residual CO_2 flow in the outlet of cathode chamber and gas flow chamber, which is determined by GC. CO_2 in electrolyte is the residual CO_2 in electrolyte in form of (bi)carbonate.

Supplementary references

1. Jiang, S. *et al.* Investigation of cobalt phthalocyanine at the solid/liquid interface by electrochemical tip-enhanced Raman spectroscopy. *J. Phys. Chem. C* **123**, 9852-9859 (2019).
2. Chen, Z. *et al.* Operando characterization of iron phthalocyanine deactivation during oxygen reduction reaction using electrochemical tip-enhanced Raman spectroscopy. *J. Am. Chem. Soc.* **141**, 15684-15692 (2019).
3. The National Institute of Standards and Technology. NIST Standard Reference Database Number 69. NIST Chemistry WebBook (2018).
4. Wiesenburg, D.A., and Guinasso, N.L. Equilibrium solubilities of methane, carbon monoxide, and hydrogen in water and sea water. *J. Chem. Eng. Data* **24**, 356-360 (1979).
5. Weisenberger, S., and Schumpe, A. Estimation of gas solubilities in salt solutions at temperatures from 273 K to 363 K. *AIChE J.* **42**, 298-300 (1996).
6. McCallum, C. *et al.* Reducing the crossover of carbonate and liquid products during carbon dioxide electroreduction. *Cell Rep. Phys. Sci.* **2**, 100522 (2021).
7. Li, F., Zhou, C. & Klinkova, A. Simulating electric field and current density in nanostructured electrocatalysts for CO_2 reduction. *Phys. Chem. Chem. Phys.,* **24***,* 25695-25719 (2022).
8. K. Tanaka and M. Nomura, Measurements of Tracer Diffusion Coefficients of Lithium Ions, Chloride Ions and Water in Aqueous Lithium Chloride Solutions, *J. Chem. Soc., Faraday Trans.* **1**, 83, 1779–1782 (1987).
9. Mohammad, M.; Tariq, M.; Qadri, M.; Latif, M.; Tahiri, I.; Naz, L. Diffusion Coefficient of Iodide Ions in Aqueous Medium and in Vacuum: *An Appraisal. J.-Chem. Soc. Pak.* 37 (2015).
10. Cantrel L. Diffusion coefficients of molecular iodine in aqueous solutions. *J. Chem. Eng. Data.* **42**, 216-220 (1997).
11. Huang, J.E. et al. CO_2 electrolysis to multicarbon products in strong acid. *Science* **372**, 1074-1078 (2021).
12. Dinh, C.-T. et al. CO_2 electroreduction to ethylene via hydroxide-mediated copper catalysis at an abrupt interface. *Science* **360**, 783-787, (2018).

13. Weng, L. C., Bell, A. T. & Weber, A. Z. Modeling gas-diffusion electrodes for CO_2 reduction. *Phys. Chem. Chem. Phys.* **20**, 16973-16984, (2018).

14. Ozden, A. et al. Cascade CO_2 electroreduction enables efficient carbonate-free production of ethylene. *Joule* **5**, 706-719 (2021).

15. Ozden, A., García de Arquer, F.P., Huang, J.E. et al. Carbon-efficient carbon dioxide electrolysers. *Nat. Sustain.* **5,** 563-573 (2022).

16. Russel, I. Undserstanding yeast fundamentals, The Alcohol Textbook, Chapter **9**, 85-119 (2003).

17. Li, F. et al. Molecular tuning of CO_2-to-ethylene conversion. *Nature* **577**, 509-513 (2020).

18. Ma, M. *et al.* Insights into the carbon balance for CO_2 electroreduction on Cu using gas diffusion electrode reactor designs. *Energy Environ. Sci.* **13**, 977-985 (2020).